

Discovery of a Hematopoietic Manifold in scGPT Yields a Method for Extracting Performant Algorithms from Biological Foundation Model Internals

Ihor Kendiukhov¹

¹Department of Computer Science, University of Tübingen, Tübingen, Germany
kendiukhov@gmail.com

Abstract

We report the discovery and extraction of a compact hematopoietic algorithm from the single-cell foundation model scGPT—to our knowledge, the first biologically useful, competitive algorithm extracted from a foundation model via mechanistic interpretability. We show that scGPT internally encodes a compact (~ 8 – 10 -dimensional) hematopoietic manifold with significant developmental branch structure, validated on a strict non-overlap Tabula Sapiens external panel (616 anchors, 564,253 cells) and confirmed via frozen-head zero-shot transfer to an independent multi-donor immune panel (trustworthiness 0.993, blocked-permutation $p=0.0005$). To isolate this geometry, we introduce a general three-stage extraction method—direct operator export from frozen attention weights, lightweight learned adaptor, and task-specific readout—that produces a standalone algorithm without target-dataset retraining. In 88-split donor-holdout benchmarks against scVI, Palantir, DPT, CellTypist, PCA, and raw-expression baselines, the extracted algorithm achieves the strongest pseudotime-depth ordering (orientation-independent $|\rho|=0.439$ versus 0.331 for the next-best alternative; Wilcoxon BH- $q \leq 2.7 \times 10^{-7}$ on all paired comparisons) and leads on key subtype endpoints (CD4/CD8 AUROC 0.867, mono/macro AUROC 0.951). Compared to standard probing of frozen scGPT embeddings with a 3-layer MLP (172k parameters), the extracted head is BH-significantly better on 6/8 classification endpoints while completing a full 12-split evaluation campaign $34.5\times$ faster (~ 3.4 versus ~ 118 minutes) with $\sim 1,000\times$ fewer trainable parameters. The exported operator compresses from three pooled attention heads to a single head (L2H5; 17.5 \rightarrow 5.9 MB) without statistically significant loss, and further to a rank-64 surrogate (0.73 MB). Mechanistic interpretability of the compact operator reveals a concentrated four-factor core explaining 66.2% of ablation impact, with factors resolving into explicit T/lymphoid, B/plasma, granulocytic, and monocyte/macrophage gene programs. A supplementary second-manifold validation (intercellular communication geometry) confirms that the extraction method generalizes beyond hematopoiesis.

1 Introduction

Foundation models for biology are increasingly powerful but largely opaque. Built on the transformer architecture [62], single-cell foundation models such as scGPT [10], Geneformer [58], scBERT [70], scFoundation [21], and UCE [49] build on earlier latent-variable approaches like scVI [31, 16] to learn rich representations of cellular state. Yet the question of *what biological knowledge these models actually encode*—and whether it can be extracted and reused—remains largely open, motivating the application of mechanistic interpretability methods [41, 12] to biological foundation models. Mechanistic interpretability has made rapid progress in language models, revealing superposition phenomena [13], complete circuits for specific behaviors [66, 39], methods for automated neuron

interpretation [5], and evidence for linear geometric structure in learned representations [43]. In biological models specifically, attention analysis of protein language models has shown that transformer heads can encode meaningful biochemical relationships [65, 7]. Recent work on single-cell foundation models has begun probing what these models learn: systematic evaluation of attention patterns in scGPT and Geneformer revealed that attention captures gene co-expression structure rather than unique regulatory signal, with simple gene-level baselines dominating pairwise attention edges for perturbation prediction [24]. Sparse autoencoder decomposition of both models uncovered over 107,000 interpretable features organized into biological pathways, yet only 6.2% of transcription factors showed regulatory-target-specific responses, indicating minimal causal regulatory logic [26]. Causal circuit tracing further revealed that both architectures converge on inhibitory-dominant computational motifs with approximately 53% biological coherence, suggesting shared representational principles across model families [25]. However, the question of whether the structured biological knowledge these models *do* encode can be extracted as a reusable algorithm has not been addressed.

A key precedent comes from protein language models. Protein structure prediction [23] and evolutionary sequence models [48, 30, 40] have demonstrated that large-scale pretraining captures deep biological structure. The Goodfire phylogeny-manifold program showed that Evo2 [40] internally encodes a compact manifold corresponding to the evolutionary tree of life, recoverable through rigorous geometric auditing with external biological rulers [45, 48, 30]. That result established that biologically meaningful manifolds can be discovered inside foundation models. More broadly, methods for localizing knowledge in specific transformer components [37, 18] and for discovering causal structure through intervention [17] provide a methodological foundation for the extraction approach we pursue here.

We ask: can we go further? Specifically, can we (i) discover analogous biological manifolds in single-cell foundation models, (ii) extract them as reusable algorithms, and (iii) compress them into compact, interpretable operators? This paper answers all three questions affirmatively for hematopoiesis in scGPT, yielding what is, to our knowledge, the first competitive algorithm extracted from a foundation model via mechanistic interpretability.

Our approach connects to the rich tradition of geometric manifold learning [57, 50, 8, 36, 38] and trajectory inference in single-cell biology [60, 46, 19, 53, 69, 51], including RNA velocity approaches [28, 4], single-cell data integration methods [54, 27, 34], and reference-atlas transfer learning [32]. However, rather than fitting manifolds to observed gene expression, we extract geometric structure from the *internal* attention operators of a pretrained model and evaluate it under strict holdout, confound, and external-transfer controls. For biological grounding, we use Tabula Sapiens [55], part of the broader Human Cell Atlas effort [47], and curated regulatory resources [15, 20]. The discovery was conducted through a two-phase autonomous research loop: a broad hypothesis search that screened dozens of candidates against pre-registered quality gates, followed by focused investigation of the surviving positive branch (Section 2.1).

Main contributions.

1. **Manifold discovery.** We discover a compact hematopoietic manifold in scGPT, validated internally (trustworthiness 0.993, blocked-permutation $p=0.0005$) and externally on a strict non-overlap Tabula Sapiens panel (616 anchors, 564,253 cells) and a separate multi-donor panel in frozen zero-shot mode.
2. **Extraction method.** We introduce a three-stage pipeline—direct operator export, lightweight learned adaptor, task-specific readout—that isolates transferable biological geometry from frozen model weights without target-dataset retraining.

3. **Competitive extracted algorithm.** The extracted algorithm significantly outperforms scVI, Palantir, DPT, CellTypist, PCA, and raw-expression baselines on pseudotime-depth alignment (88 donor-holdout splits; all paired BH- $q \leq 2.7 \times 10^{-7}$) and leads on key subtype classification endpoints.
4. **Multi-stage compaction.** The exported operator compresses from pooled attention heads to a single head (L2H5; 17.5 \rightarrow 5.9 MB) without significant loss, and further to a rank-64 surrogate (0.73 MB).
5. **Mechanistic interpretability.** Factor ablation and sparse factorization of the compact operator reveal a four-factor core (66.2% of ablation impact) resolving into explicit hematopoietic gene programs, providing among the most detailed mechanistic decompositions of a foundation-model-derived algorithm.

2 Methods

2.1 Autonomous research loop

The study was conducted through a two-phase autonomous research loop driven by an AI executor–reviewer pair operating under pre-registered quality gates, extending the emerging paradigm of AI-driven scientific discovery [33].

Phase 1: Broad hypothesis search. The loop explored a large space of candidate manifold hypotheses by systematically varying biological targets (developmental ordering, regulatory structure, communication geometry), featurization strategies (attention drift, raw embeddings, mixed operators), and geometric fitting methods (Isomap, geodesic-MDS, LET) across the scGPT attention tensor. Each candidate was evaluated against fixed quantitative gates—trustworthiness ≥ 0.80 , holdout correlation ≥ 0.20 on random/donor/clade splits, and blocked-permutation $p \leq 0.001$ —with an adversarial reviewer role rejecting candidates that failed any gate or showed confound sensitivity. This phase operated at scale: dozens of hypothesis branches were instantiated, tested, and rejected before a positive signal emerged. The key output of Phase 1 was the identification of hypothesis H65 (hematopoietic developmental manifold) as the first branch to pass all gates with a robust positive signal, while a paired null branch (H66, same pipeline with a different biological target) failed, confirming that the signal was branch-specific rather than a pipeline artifact.

Phase 2: Focused investigation. Once the autonomous loop identified H65 as a robust positive branch, the research transitioned to manual, author-led investigation. This phase included: methodological closure tests (objective ablations, confidence intervals, structured holdouts), strict non-overlap external transfer validation, extraction and benchmarking of the manifold as a standalone algorithm, multi-stage operator compaction, and mechanistic interpretability via factor ablation and sparse factorization. While the same quantitative gate logic from Phase 1 was retained as a quality standard, the experimental design, analysis, and interpretation in Phase 2 were conducted by the authors rather than by the autonomous loop. A second branch (H38, intercellular communication geometry) was also carried through both phases as an independent generalization test (Supplementary S32–S37). Full iteration logs and the Phase 1 search trajectory are documented in Supplementary S1.

2.2 Data and anchor construction

We derived donor \times tissue \times cell-type **anchors**—aggregate representations (centroids) computed by averaging scGPT embeddings over all cells sharing a donor, tissue, and cell-type label—from

Tabula Sapiens [55] immune data processed through the frozen scGPT whole-human checkpoint [10]. The **internal panel** used 298 anchors across 7 hematopoietic branch groups (5 tissues). The **strict non-overlap external panel** was built by excluding all internal observation IDs, mapping remaining cells to the same stage ontology, and aggregating: 564,253 cells, 616 anchors, 21 donors, 27 tissues, 34 fine stages across 7 branches. A separate **multi-donor immune panel** (7 cohorts, 165 anchors, 10,819 sampled cells) was reserved for frozen zero-shot transfer confirmation (protocol in Supplementary S4). No external data were used during any training step.

2.3 Three-stage extraction pipeline

We treat the manifold as an extracted algorithm rather than a visualization artifact:

$$x \xrightarrow{\text{Stage 1: frozen operator}} f(x) \xrightarrow{\text{Stage 2: learned adaptor } g_\theta} z \xrightarrow{\text{Stage 3: task readout } h_\phi} \hat{y}.$$

Stage 1: Direct operator extraction. From the frozen scGPT checkpoint, we read native attention operators $A_{\ell,h} \in \mathbb{R}^{1200 \times 1200}$ (the value-projection weight matrices from layer ℓ , head h , which define how each gene’s embedding is linearly transformed within that head) and construct a fixed feature map. The main benchmark uses a pooled drift operator:

$$f_{\text{drift}}(x) = [(xA_{\text{early}} - xA_{\text{mid}}) ; (xA_{\text{mid}} - xA_{\text{late}})] \in \mathbb{R}^{2400},$$

where $A_{\text{early}}, A_{\text{mid}}, A_{\text{late}}$ average native heads over early, middle, and late layer blocks. The intuition is that successive transformer layers progressively refine gene representations; the pairwise differences capture how each cell’s representation *changes* across layers, and this representational drift may encode developmental trajectory information. No target labels are used; no parameters are optimized.

Stage 2: Lightweight learned adaptor. A small head g_θ is trained on internal data only, mapping fixed features to a task-agnostic manifold latent z ($d = 10$). We use a Latent Embedding Transfer (LET) objective:

$$z = W_{\text{enc}}(x - b), \quad \hat{d}_{ij} = \beta \arccos(\cos(z_i, z_j)), \tag{1}$$

$$\mathcal{L} = \|\hat{d} - d_{\text{target}}\|^2 + \alpha \|W_{\text{enc}}^+ z + b - x\|^2. \tag{2}$$

Here d_{target} are pairwise biological distances derived from a curated hematopoietic stage ontology (e.g., the number of developmental steps separating two cell types), so the first term encourages the latent geometry to reflect developmental proximity, and the second term is a reconstruction regularizer. Quality gates require trustworthiness (a measure of local neighborhood preservation: the fraction of each point’s nearest neighbors in the high-dimensional input that remain neighbors in the low-dimensional embedding [64]) ≥ 0.80 and random/donor/clade holdout correlations ≥ 0.20 (full equation-level details in Supplementary S3). We trained three head variants: an anchor-trained head, a cell-trained head (6,925 cells, stage-balanced), and a hybrid head with topology preservation (Supplementary S5–S6). An artifact-closure protocol ensured that all claims survive structured holdout and permutation controls (Supplementary S2).

Stage 3: Task-specific readout. Small probes h_ϕ are trained on top of z for classification or pseudotime regression. These are not part of the shared representation.

2.4 Head/layer attribution and multi-stage compaction

Drawing on methods for localizing factual knowledge in specific model components [37, 18], we scanned all 96 units of the 12×8 scGPT attention tensor. Each unit (ℓ, h) was evaluated via

single-head feature map $x \mapsto xA_{\ell,h}$ with LET-10D trained on internal anchors and tested zero-shot on external anchors. Compact operators replace the pooled drift map with a weighted sum of top-ranked heads:

$$\tilde{A}_k = \sum_{i=1}^k \alpha_i A_{\ell_i, h_i}.$$

Further compression uses truncated-SVD surrogates $\tilde{A}_k \approx U_r V_r^\top$ ($r \in \{8, 16, 32, 64\}$) and hard sparse pruning (top- k read and write genes per retained factor, where “read genes” are those with highest input loadings and “write genes” are those with highest output loadings in each rank-1 factor of the SVD). Each compression stage retrains only the lightweight adaptor and task probes. Factor necessity was assessed via fixed-probe leave-one-out ablation. Terminology, compression stages, and the full operator hierarchy are detailed in Supplementary S12.

2.5 Benchmark evaluation protocol

We benchmarked extracted heads against raw-expression (1200 $\log(1+x)$ genes), PCA-10, SVD-10, CellTypist [11], scVI-10D [31], Scanpy-DPT [68, 19], and Palantir [52] on the strict non-overlap external panel. The finalized Robust-V2 campaign used 88 grouped donor-holdout splits (100,000 training cells per split). Metrics: branch/stage balanced accuracy and macro-F1, CD4/CD8 and mono/macro AUROC, and pseudotime-depth Spearman correlation (the rank correlation between the inferred pseudotime ordering and the known ontology-based developmental stage depth). All pseudotime was evaluated with donor-local test-only protocol. Paired statistical comparisons used split-level Wilcoxon signed-rank tests with Benjamini–Hochberg false discovery rate (BH-FDR) correction [3]. Statistical controls and robustness tests (confidence intervals, structured holdout correlations) are detailed in Supplementary S7; full benchmark protocol details in Supplementary S8. Additional ablations (embedding baselines, probe-depth variants, direct-MLP learnability) are reported in Supplementary S19–S22.

3 Results

3.1 Discovery of a hematopoietic manifold in scGPT

The Phase 1 broad search (Section 2.1) converged on hypothesis H65 as the robust positive branch after rejecting dozens of alternative candidates. On the internal panel, H65 achieved high manifold fidelity (trustworthiness 0.993, geodesic–biological correlation 0.835, blocked-permutation $p=0.0005$), while a paired null branch (H66) failed gates. The manifold exhibits distinct hematopoietic branch structure (Figure 1) with significant developmental ordering along erythroid ($\rho=0.768$, $p=0.0017$), granulocytic ($\rho=0.568$, $p=0.0033$), and trunk HSC/HPC/CMP (hematopoietic stem cell / hematopoietic progenitor cell / common myeloid progenitor; $\rho=0.611$, $p=0.018$) trajectories (Supplementary S13). The recovered branch structure aligns with the established hierarchical model of hematopoiesis [42, 29], including the continuous lineage commitment observed in progenitor populations [63, 44] and the direct link between transcriptional state and cell fate established by clonal barcoding [67]. The effective dimensionality is ~ 8 –10: external transfer objective and trustworthiness both improve from $d=3$ through $d=10$ (Supplementary S14).

3.2 External validation and zero-shot transfer

A small independent lung panel showed strong global association but failed robust transfer gates (low trustworthiness, weak clade transfer). In contrast, the strict non-overlap Tabula Sapiens panel

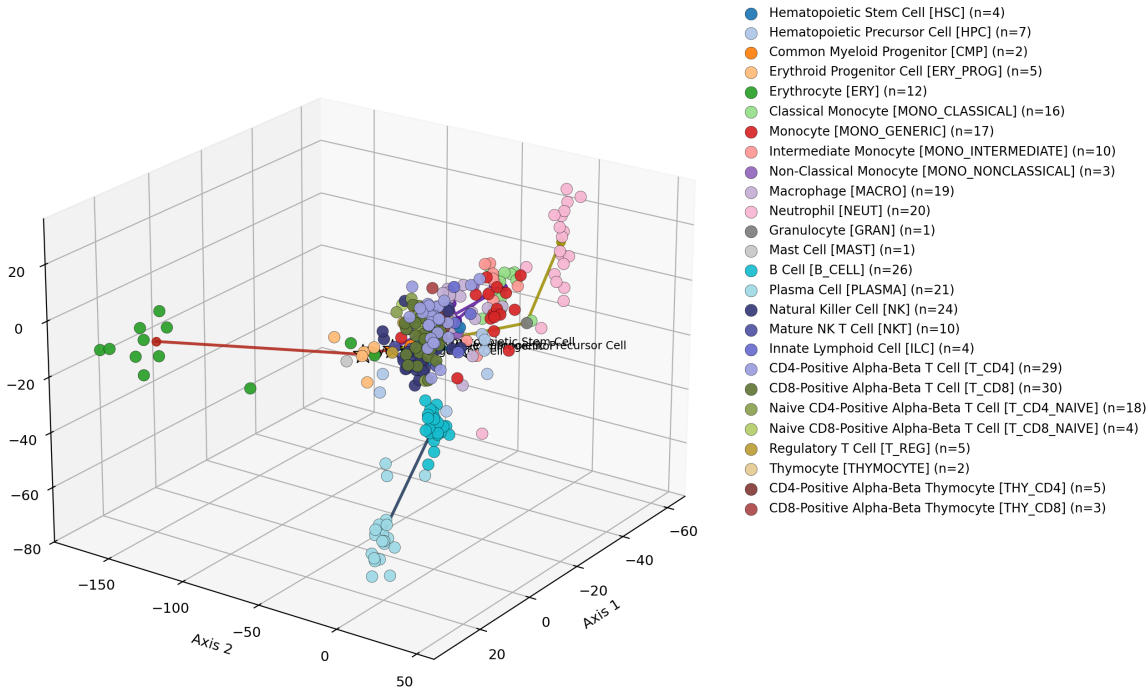


Figure 1: Hematopoietic manifold discovered in scGPT attention geometry (internal panel). Distinct branch structure emerges around stem/progenitor, erythroid, granulocytic, monocyte/macrophage, and lymphoid/T-cell regions.

Table 1: LET holdout robustness under shared gates. Trust. = trustworthiness; Random/Donor/Branch = Spearman correlation between predicted and target distances on random, donor-held-out, and branch-held-out test splits, respectively.

Panel	Trust.	Random	Donor	Branch
Internal (H65, $d=10$)	0.979	0.495	0.496	0.382
External lung ($d=6$)	0.617	0.236	0.687	0.058
External Tabula non-overlap ($d=10$)	0.985	0.594	0.596	0.453

passed all gates under the same LET protocol (Table 1). A separate frozen-head zero-shot test on an independent multi-donor immune panel (7 cohorts, 165 anchors) further confirmed transferability without any retraining (Table 2).

We trained three head variants via Stage 2 of the extraction pipeline: an anchor-trained head, a cell-trained head (6,925 cells), and a hybrid head with topology preservation. The cell-trained head improved subtype separability (CD4/CD8 AUC 0.744→0.886, mono/macro AUC 0.759→0.937) at a small cost in branch compactness; the hybrid head offered a Pareto tradeoff favoring branch readability (Supplementary S15–S16).

3.3 The extracted algorithm is competitive

We evaluated the extracted manifold head as a standalone algorithm against established methods. Table 3 reports the finalized Robust-V2 benchmark (88 grouped donor-held-out splits, 100k training

Table 2: Frozen-head zero-shot transfer on a separate external multi-donor panel.

Panel	Anchors	Donors	Stages	Corr	Corr _{resid}	Trustworthiness	Blocked p
External multi-donor zero-shot	165	7	7	0.500	0.476	0.993	0.0005

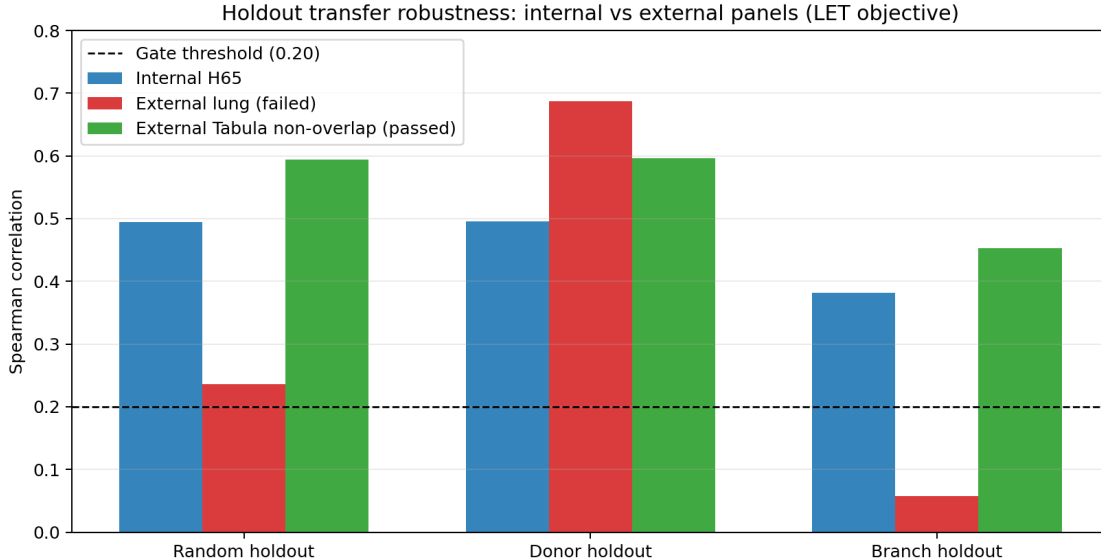


Figure 2: Holdout transfer comparison. The strict non-overlap external panel passes all gates, while the lung panel fails robust transfer despite strong global association.

cells per split, donor-local test-only pseudotime).

Classification remains mixed by endpoint. Stage/branch macro-F1 is highest for diffusion-style baselines (Palantir and Scanpy-DPT), while raw-expression is highest on stage balanced accuracy. The extracted cell head remains strongest on branch balanced accuracy, CD4/CD8 AUROC, and mono/macro AUROC.

For pseudotime-depth ordering, the extracted cell head leads all compared methods. Because pseudotime orientation is arbitrary across donor-local evaluations (each donor’s pseudotime is computed independently, and the algorithm may assign increasing values toward either stem or mature cells), we report the orientation-independent $|\rho|$ (see Section 5 for the full orientation analysis): the cell head achieves $|\rho|=0.439$ versus 0.364 (hybrid), 0.331 (Palantir), 0.279 (SVD), 0.274 (scVI), 0.266 (raw), 0.261 (DPT), 0.259 (PCA), 0.253 (CellTypist), and 0.235 (anchor). In paired split-level tests versus the cell head, all method-minus-head deltas are negative with Wilcoxon BH- $q \leq 2.7 \times 10^{-7}$ in the 88-split pooled analysis (Table 4 and Figure 3).

The extraction gain is not reducible to trivially fitting a small MLP on raw expression. A direct raw-expression MLP (1200→64) learns substantial stage signal (stage balanced accuracy 0.499–0.504 versus 0.468 for the extracted head) but fails to match the extracted head’s subtype-sensitive advantages: CD4/CD8 AUROC 0.828 versus 0.856, mono/macro AUROC 0.920–0.926 versus 0.956 (all BH-significant; Supplementary S22). The scGPT-derived geometric structure provides subtype separation that raw-expression probes cannot recover.

A stronger test asks whether the advantage persists when frozen scGPT embeddings are paired with a deeper non-linear readout. In 12-split repeated evaluation, a frozen scGPT avg-pool embedding with a 3-layer MLP (172k–175k trainable parameters) is BH-significantly worse than

Table 3: Large-cell Robust-V2 pooled donor-holdout benchmark on strict non-overlap mapped cells (100k training cells per split). Values are pooled donor-level means across 88 grouped splits. Coverage varies by method/metric due to valid-run filtering (pseudotime: 88 splits for most methods, 70 for Palantir, 36 for scVI).

Method	Branch bal. acc.	Branch macro-F1	Stage bal. acc.	Stage macro-F1	CD4/CD8 AUROC	Mono/Macro AUROC	Pseudotime Spearman
H65 anchor head (10D)	0.750	0.557	0.465	0.184	0.803	0.934	0.093
H65 cell head (10D)	0.828	0.584	0.552	0.216	0.867	0.951	0.249
H65 hybrid conservative (10D)	0.815	0.599	0.542	0.217	0.858	0.949	0.132
Raw baseline (1200 log1p)	0.826	0.595	0.567	0.219	0.805	0.833	-0.044
PCA-10 baseline	0.733	0.543	0.503	0.194	0.842	0.944	-0.007
SVD-10 baseline	0.731	0.541	0.499	0.192	0.842	0.936	0.002
CellTypist stage-probability baseline	0.703	0.588	0.393	0.226	0.785	0.855	-0.064
scVI-10D baseline	0.793	0.551	0.512	0.205	0.849	0.916	-0.103
Scanpy-DPT baseline	0.750	0.606	0.451	0.235	0.793	0.947	-0.089
Palantir baseline	0.759	0.621	0.423	0.242	0.750	0.946	-0.049

Table 4: Robust-V2 paired pseudotime statistics versus H65 cell head (split-level mean differences; method minus cell head).

Method	n_{splits}	Mean diff	Wilcoxon BH- q
H65 hybrid conservative (10D)	88	-0.056	2.7×10^{-7}
H65 anchor head (10D)	88	-0.092	2.7×10^{-7}
SVD-10 baseline	88	-0.185	9.7×10^{-15}
PCA-10 baseline	88	-0.194	2.6×10^{-14}
Raw baseline (1200 log1p)	88	-0.226	2.5×10^{-14}
CellTypist stage-probability baseline	88	-0.260	7.0×10^{-15}
scVI-10D baseline	36	-0.261	4.1×10^{-9}
Scanpy-DPT baseline	88	-0.272	2.6×10^{-14}
Palantir baseline	70	-0.293	3.7×10^{-12}

the extracted 10D head on 6/8 endpoints, including branch macro-F1 ($\Delta=-0.045$, BH- $q=0.010$) and stage macro-F1 ($\Delta=-0.078$, BH- $q=0.0013$); the deeper MLP matches or closes the gap only on CD4/CD8 and mono/macro AUROC (Supplementary S19–S20). When reducing to a comparable 4D head, the extracted operator wins on 5/8 endpoints with BH correction. A probe-depth sweep on the extracted head itself (Supplementary S21) shows that a 2-layer MLP readout yields BH-significant gains on CD4/CD8 AUROC (+0.0045) but worsens stage endpoints, confirming that the linear default is a robust Pareto choice.

Beyond accuracy, the extracted head is substantially faster. One-time preparation (drift operator computation and LET head training) takes ~ 100 seconds versus $\sim 5,164$ seconds for running all cells through the frozen scGPT encoder to obtain embeddings—a $52\times$ gap. Per-split training costs ~ 9 seconds (2 s probe training + 7 s drift-feature inference) versus ~ 159 seconds for the 3-layer MLP ($18\times$), and the full 12-split campaign completes in ~ 205 seconds versus $\sim 7,074$ seconds ($34.5\times$ faster). The extracted head requires only 5–170 trainable parameters per downstream task, versus 172k–175k for the frozen-embedding MLP path (Supplementary S23).

Table 5 consolidates these comparisons across performance, training cost, and deployment footprint. The frozen scGPT path additionally requires running all ~ 140 k cells through the full 12-layer transformer to obtain embeddings (~ 86 minutes), making it the most expensive preparation step by far. The direct raw-expression MLP avoids scGPT entirely but requires ~ 120 – 188 s per split due to its 1,200-dimensional input, and cannot recover the subtype geometry that scGPT’s internal representations provide.

Unsupervised branch recovery, by contrast, is a weakness. When the extracted head’s output is fed through standard unsupervised wrappers (Scanpy Leiden+PAGA or Palantir fate assignment),

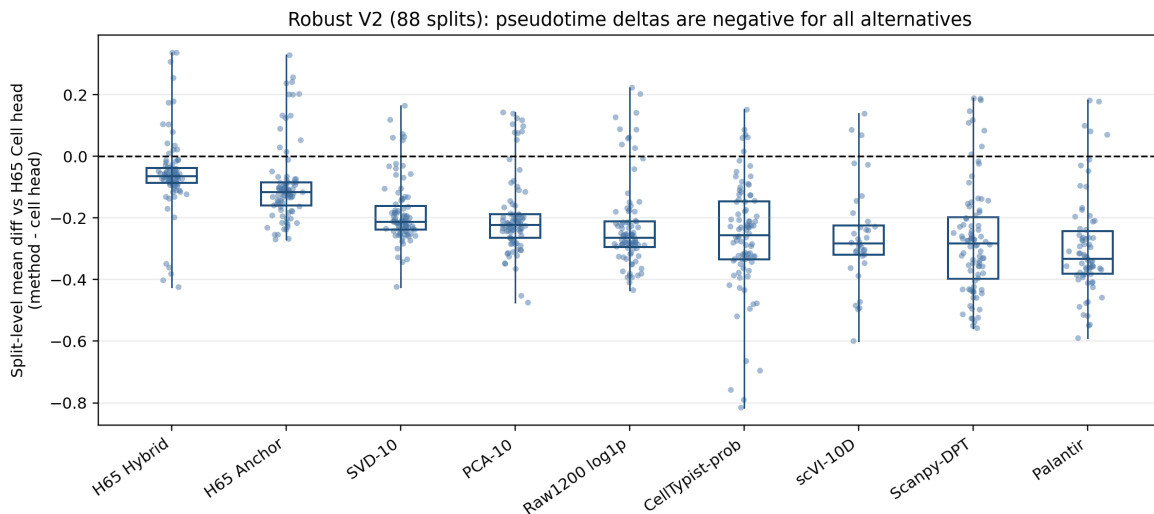


Figure 3: Robust-V2 split-level pseudotime deltas versus H65 cell head (method minus cell head). All alternatives are below zero.

Table 5: Summary comparison of the three evaluated approaches on the 12-split repeated benchmark. Performance values are pooled donor-level means. Training times from Supplementary S23; parameter counts from model architectures. BH-sig. wins/losses count endpoints (out of 8) on which the method is BH-significantly better/worse than the extracted head.

	Extracted 10D head + MLP2	Frozen scGPT + 3-layer MLP	Direct raw MLP (128→64)
<i>Key classification metrics</i>			
Branch bal. acc.	0.827	0.810	0.818
Stage bal. acc.	0.468	0.403	0.504
CD4/CD8 AUROC	0.856	0.817	0.827
Mono/Macro AUROC	0.956	0.946	0.920
<i>Training and deployment cost</i>			
One-time preparation	100 s (drift + head)	5,164 s (encoder fwd pass)	172 s (log-normalize)
Per-split training	2 s (probe) + 7 s (inference)	159 s (MLP training)	120–188 s (MLP training)
Full 12-split campaign	~205 s (~3.4 min)	~7,074 s (~118 min)	~1,600–2,400 s
Trainable parameters / task	5–170	172,610–174,690	77,000–164,000
Deployable artifact	5.9 MB (compact head)	~400 MB (frozen encoder)	<1 MB
BH-sig. wins vs extracted head	—	0 / 8	2 / 8 (stage only)
BH-sig. losses vs extracted head	—	6 / 8	3 / 8 (subtype)

raw expression performs comparably or better on partition metrics such as the Adjusted Rand Index (ARI). The extracted head’s advantage is concentrated in supervised classification and pseudotime ordering, not in unsupervised topology recovery (Supplementary S18).

3.4 Multi-stage compaction

To localize the biological signal within scGPT, we scanned all 96 attention heads (12 layers \times 8 heads). A single head—Layer 2, Head 5 (L2H5)—carried the strongest transferable developmental geometry (residualized correlation 0.634, i.e., the correlation between predicted and target distances after regressing out donor and tissue confounds; trustworthiness 0.985), competitive with the three-head pooled variants (pooled-anchor 0.605, pooled-cell 0.612, hybrid 0.632; Supplementary S29). Pooled heads retain an advantage on subtype margins (CD4/CD8 AUROC 0.911 hybrid versus

Table 6: Compaction chain: from pooled drift operator to single-head and low-rank surrogates. Losses are relative to the full extracted 10D head under paired BH-corrected tests.

Operator variant	Size	BH-sig. losses (of 8)	Key note
Full drift (3 pooled heads)	17.5 MB	—	Reference
Compact top1 (L2H5)	5.9 MB	0/8	Best single head
Top1 + rank 64	0.73 MB	5/8	Viable low-rank boundary
Top1 + rank 32	0.37 MB	6/8	Degraded
Hard sparse (16 factors, 60 genes)	0.12 MB	7/8	Interpretable, baseline-level

0.711 L2H5 in 3D), motivating their use in the benchmark, but the single-head result shows the signal is surprisingly localized. The compact operator $\hat{A}_1 = \alpha_1 A_{2,5}$ preserves classification utility without BH-significant loss on all eight repeated endpoints, while reducing the deployable artifact from ~ 17.5 MB (three pooled heads) to ~ 5.9 MB (Table 6).

Further compression via truncated-SVD yields viable surrogates down to rank 64 (0.73 MB), though with BH-significant losses on 5/8 endpoints versus the dense compact operator. More aggressive ranks (32, 16, 8) degrade substantially. Hard sparse pruning (16 factors, 60 read/write genes each; 124 KB deployable package) yields an interpretable but baseline-level-accuracy surrogate.

3.5 Mechanistic interpretability of the compact operator

The rank-64 low-rank factorization (via truncated SVD, yielding 64 rank-1 components, each defined by a pair of input and output gene-loading vectors) enables direct mechanistic analysis. Fixed-probe leave-one-factor-out ablation reveals highly concentrated necessity: the top four factors (f01, f02, f00, f03) explain 66.2% of total pooled ablation impact (the summed classification accuracy drop across all endpoints when a factor is removed) (Figure 4). A core-sufficiency test shows that this four-factor subset is necessary but not sufficient: branch balanced accuracy drops from 0.820 (intact rank-64) to 0.572 (four-factor core), CD4/CD8 AUROC from 0.846 to 0.699, and all eight endpoints are BH-significantly worse than the intact model (Supplementary S30). An exhaustive 15-subset interaction sweep over the four core factors reveals task-specialized circuitry rather than a monotone additive ladder: branch/stage classification is best served by the full four-factor set, while mono/macro separation peaks at the pair {f01, f03} (AUROC 0.902, 94.9% of intact) and CD4/CD8 at a triple centered on f00+f03 (AUROC 0.703, 83.1% of intact).

Cached local marker enrichment and external pathway analysis using Gene Ontology annotations [1] resolve these core factors into explicit biological programs (Table 7):

- **f01**: branch-routing factor, dominant on branch classification; monocyte/macrophage-aligned markers.
- **f02**: lymphoid contrast factor; B-cell versus T/NK separation.
- **f00**: strongest stage signal; granulocytic/T-NK developmental axis.
- **f03**: monocyte/macrophage versus granulocytic structure.

The same four-factor core persists in the hard-sparse surrogate (16 factors, 60 read/write genes), where it explains 68.9% of sparse-specific ablation impact. Read/write gene overlaps between the rank-64 and sparse factorizations confirm that the same mechanistic substrate survives aggressive compression (Supplementary S27–S28).

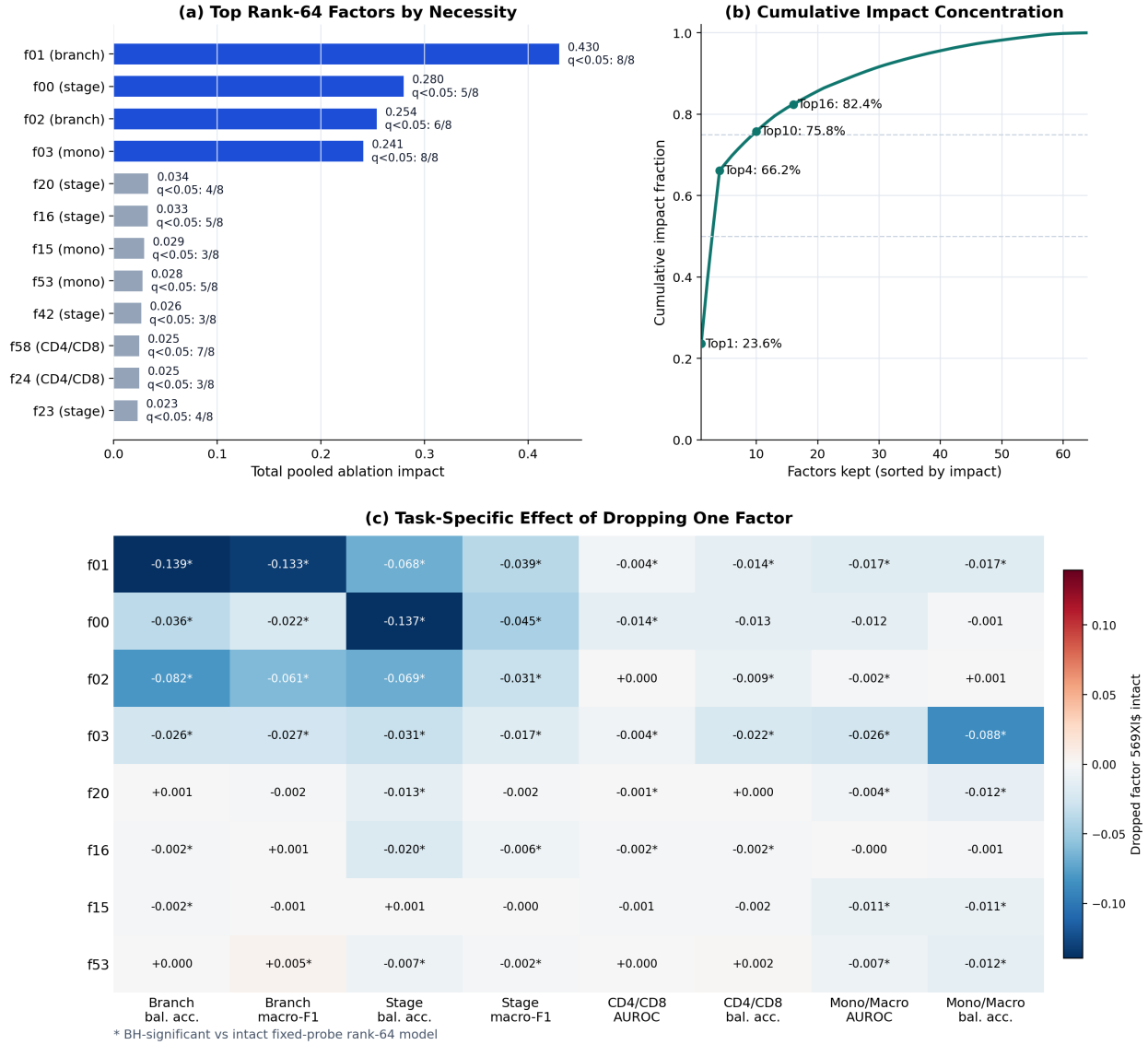


Figure 4: Fixed-probe leave-one-factor-out ablation for the rank-64 compact operator. (a) Total pooled ablation impact for the 12 most impactful factors. (b) Cumulative concentration curve—the top four factors explain 66.2% of total ablation impact. (c) Per-task drop magnitudes; asterisks denote BH-significant loss versus the intact model.

Table 7: Gene-program summary for the four core factors of the rank-64 compact operator. Ablation drop is the total pooled classification loss when the factor is removed. Top read/write genes and enriched marker sets are from cached local marker enrichment.

Factor	Role	Drop	Top read/write genes	Enriched programs
f01	Branch routing	0.430	R: CSF3R, SLC6A1, IL7R; W: CSF3R, SLC25A37, FCER1G	Mono/macro diff.; naïve CD8 ⁺ T; granulopoiesis
f02	Lymphoid contrast	0.254	R: IL7R, GSTPL, IGF2R; W: HLA-DRA, MARCH6, IGKV5	Lymphoid B vs T/NK; CD4 ⁺ T maturation
f00	Stage ordering	0.280	R: EPB41, GMR1, VPEL3; W: ISHC, LGALS14, EPB41	Classical monocyte; naïve CD8 ⁺ T program
f03	Mono/macro struct.	0.241	R: LGALS3, GT58, LYZ; W: VPEL5, ALPL, SLC28A3	Macrophage; granulocyte; B-cell markers

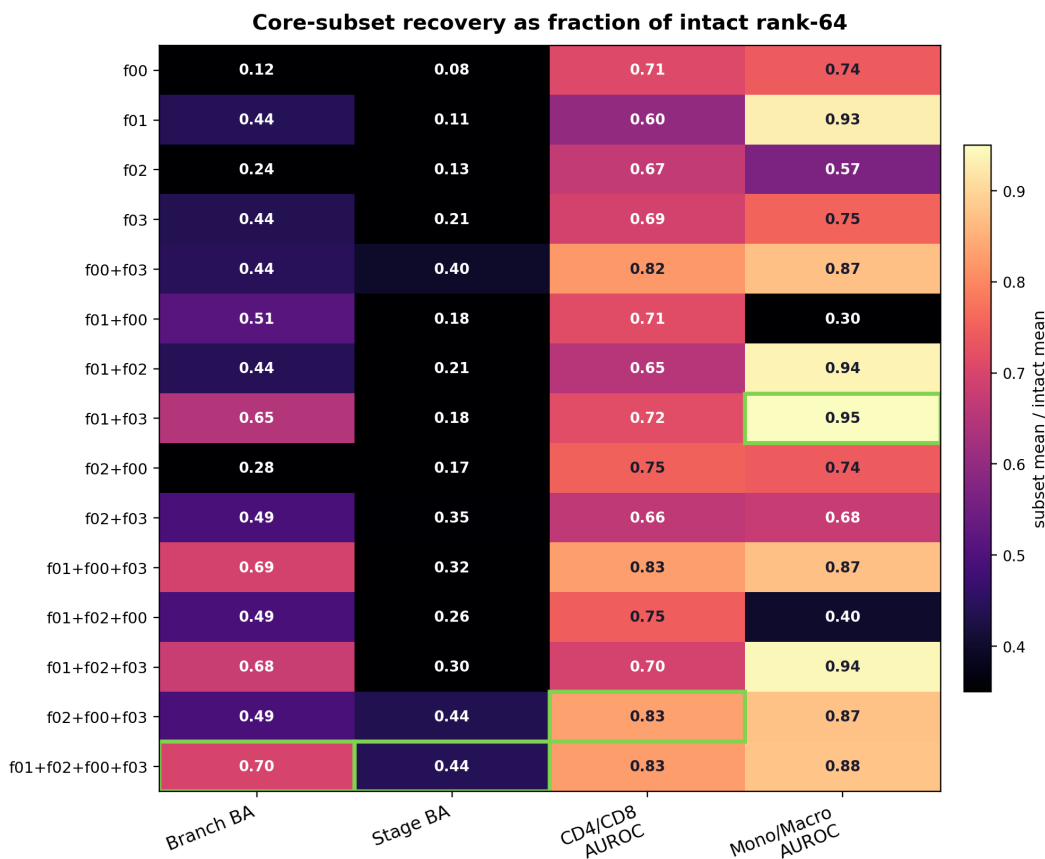


Figure 5: Core-subset recovery as a fraction of intact rank-64 performance across the exhaustive 15-subset interaction sweep. Green borders mark the best subset for each endpoint. No subset closes the gap to the intact model (all remain BH-significant); task-specialized circuitry is visible—mono/macro is well-recovered by the pair {f01, f03} alone (0.95 \times), while branch and stage require all four factors. Best subsets per endpoint are listed in Supplementary Table 22.

Latent intervention tests on the manifold (protocol in Supplementary S11) further support directional biological structure: stem \rightarrow myeloid intervention produced strong monotonic enrichment ($\rho=0.928$, $p=4.9\times 10^{-6}$), and stem \rightarrow erythroid showed a similarly strong shift ($\rho=0.739$, $p=0.0039$). The CD4 \rightarrow CD8 intervention, by contrast, was weak and non-significant ($\rho=-0.518$, $p=0.070$),

consistent with subtype-local complexity that resists simple latent-axis manipulation. Bootstrap and seed-perturbation audits confirmed stability of core claims (trustworthiness 0.979 ± 0.005 ; CD4/CD8 AUC 0.758 ± 0.013 across five seeds).

The 10D latent space distributes biological information across dimensions in a structured manner. Default 3D views under-represent T-cell subtype separability: CD4/CD8 AUROC is 0.646 in 3D but 0.822 in the full 10D latent, with the strongest single axis at dimension 4 (AUROC 0.845). Monocyte/macrophage separation peaks at dimension 8 (AUROC 0.907), and global stage/branch structure concentrates at dimension 9 (stage $\eta^2=0.952$, branch $\eta^2=0.883$, where η^2 is the ANOVA effect size measuring the proportion of variance explained by the grouping variable). A guardrailed T-cell separation lens—a visualization-only rotation that replaces one 3D axis with the most discriminative latent dimension for CD4/CD8 separation, controlled by a regularization parameter $\lambda=8$ that limits distortion of the global layout—improves CD4/CD8 AUROC from 0.835 to 0.901 while maintaining trustworthiness (methods in Supplementary S9; results in Supplementary S24). Flatness/ripple analysis (methods in Supplementary S10) shows the manifold is predominantly sheet-like (best 2D plane explains 99.25% of 3D variance) with statistically significant residual structure ($R^2=0.171$, $p=0.0033$), though residual-axis associations with curated erythroid programs did not survive BH-FDR correction (Supplementary S25–S26).

4 Discussion

The manifold is real and transferable. The hematopoietic manifold discovered in scGPT is not an internal-only artifact. Strict non-overlap external transfer preserved geometric fidelity and holdout robustness, while a separate frozen-head zero-shot test on an independent multi-donor panel remained strongly significant. The lung panel failure under the same gates demonstrates that high global correlation alone is insufficient—robust transfer requires trustworthiness and clade holdout controls.

The extracted algorithm reshapes task geometry. The standalone benchmark clarifies what the extracted algorithm does well and where it does not lead. Pseudotime-depth alignment is the cleanest advantage: the cell-trained head significantly outperforms every tested alternative in paired split-level statistics. Classification leadership is mixed—the cell head leads on branch balanced accuracy and subtype AUROCs, but diffusion-style baselines and raw expression lead on some stage/branch macro-F1 endpoints. Importantly, the extraction gain is not reducible to a trivially better probe on frozen scGPT embeddings, nor to a small MLP trained directly on raw expression (Supplementary S19–S22). The lightweight head reshapes the task geometry in ways not fully reproduced by either alternative, while requiring $34.5\times$ less compute and $\sim 1,000\times$ fewer trainable parameters than the frozen-embedding MLP path.

Compaction localizes the signal. A single attention unit (L2H5) carries substantial transferable developmental geometry, and the compact operator based on this head preserves classification utility while shrinking the artifact from 17.5 to 5.9 MB. Further compression to rank-64 (0.73 MB) remains viable at moderate cost. This progression from distributed pooled heads to a single localized operator materially strengthens the extraction claim and connects to the broader paradigm of knowledge distillation [22] and the lottery ticket hypothesis [14]: a sparse subnetwork—here a single attention head—carries the essential computation, while the remaining components contribute incremental refinement rather than qualitatively new information.

Mechanistic interpretability reaches gene-program resolution. Factor ablation and sparse factorization of the compact operator resolve a four-factor core into explicit hematopoietic gene programs. This connects to the broader mechanistic interpretability program in language models, where circuit-level analysis [41, 12, 9] and sparse dictionary learning [6, 56] have revealed interpretable computational structure, including complete circuits for specific algorithmic tasks [66, 39] and methods for tracing causal pathways through sparse feature graphs [35]. Our result represents a qualitative step beyond prior mechanistic interpretability of biological foundation models, which has typically stopped at attention pattern or embedding analyses [24]. While sparse autoencoder decomposition of these same models reveals rich biological feature organization but minimal causal regulatory logic [26], and causal circuit tracing shows convergent inhibitory-dominant architectures across model families [25], the present work demonstrates that the structured knowledge these models *do* encode—developmental geometry—can be extracted, compressed, and deployed as a competitive standalone algorithm. The core factors show task-specialized circuitry—mono/macro separation concentrates in just two factors (f01+f03), CD4/CD8 in triples centered on f00+f03, while branch and stage require the full four-factor core—rather than redundant additive structure.

A general method for extracting algorithms from biological foundation models. Beyond the specific hematopoietic result, this work demonstrates a reusable methodology for discovering and extracting biologically meaningful algorithms from the internals of biological foundation models. The three-stage extraction pipeline (operator export, learned adaptor, task readout) is model-agnostic: it requires only that the source model produces structured internal representations, and imposes no assumptions about the specific biological system. The extracted algorithms can be both more performant and dramatically faster than conventional alternatives—here, the extracted head significantly outperforms established trajectory-inference methods on pseudotime-depth alignment while completing evaluations $34.5\times$ faster and requiring $\sim 1,000\times$ fewer trainable parameters than the frozen-embedding probing path. This suggests that biological foundation models may harbor a library of compact, deployable algorithms that mechanistic interpretability can systematically surface, and that these algorithms need not be retrained or fine-tuned for each downstream application. The same protocol successfully recovered a second manifold family (intercellular communication, H38) under strict non-cheating external criteria: the final rescued variant achieved external correlation 0.983, internal trustworthiness 0.908, and a positive baseline margin (+0.006 versus PCA-2; blocked-permutation $p=0.0005$), with axes resolving cytokine/chemokine versus lipid signaling programs ($\eta^2=0.735$; Supplementary S32–S37). Our work connects to a broader tradition of analysis methods for neural language processing [2], extending these approaches from linguistic to biological domains. Methodologically, the workflow moves mechanistic interpretability from qualitative inspection toward quantitative, falsifiable geometric auditing. More broadly, manifold geometry can serve as a hypothesis engine: branch placement, axis loadings, and residual ripple structure together nominate candidate regulatory transitions that can be prioritized for targeted perturbation or longitudinal validation.

Head-training granularity. The hybrid-topology sweep extends the extraction result into an explicit optimization frontier. A stronger topology prior yields markedly cleaner branch geometry but can degrade distance-alignment fidelity; a weaker prior preserves global alignment while still improving parts of geometric readability. The Pareto structure across head variants (anchor, cell, hybrid) suggests that no single objective simultaneously maximizes all downstream endpoints, and that the choice of training granularity should be guided by the intended application.

Low-rank and sparse compression boundaries. The low-rank follow-up sharpens the boundary. A third compression step via truncated-SVD surrogates does not preserve the near-lossless behavior of the dense single-head compact operator at very low rank. The best point, top1 + rank64, still beats frozen scGPT avg-pool + MLP on all eight pooled classification endpoints and shrinks the artifact further to 0.73 MB, but it incurs BH-significant losses versus dense compact top1 on 5/8 endpoints. More aggressive ranks degrade too much. The rank64 factor-ablation audit then shows why a further compression step remains plausible: necessity is highly concentrated, with the top four factors explaining 66.2% of total pooled ablation impact and many later factors being broad but weak stabilizers. The completed sparse follow-up closes that next question more sharply. A naive hard sparse surrogate can be made extremely small (1,920 active operator weights, 124,512-byte package) but falls back to baseline-like performance. The positive result is interpretability, not frontier accuracy.

Dimensionality and geometric fine structure. “Low-dimensional” in this setting does not mean strictly 2D/3D. The data support a compact but higher-dimensional geometry: major lineage topology is visible in 3D, while full holdout-robust structure and subtype resolution are better captured in an 8–10D latent manifold. The flatness/ripple analysis refines this view: 3D maps are sheet-like with structured residuals, and latent residual-axis tests show that fine geometric structure persists directly in LET-10D representation. Ripple semantics remain unresolved: we can detect structured residual geometry reliably, but mapping those residual axes to specific curated programs is not yet significant under multiple-testing control.

Limitations. External validation covers three panels (two passing, one failing); broader cross-cohort replication would strengthen generalization claims. Biological rulers (ontology distances, regulatory priors) are proxies—no ground-truth developmental metric exists. The benchmark panel, while strong, is not exhaustive, and classification leadership remains mixed across endpoints; claims should be interpreted as benchmark-specific. Donor reuse across the 88 Robust-V2 splits is substantial (15 unique test donors), limiting the independence of split-level inference. Low-rank compression below rank-64 degrades substantially, and sparse surrogates trade accuracy for interpretability rather than preserving the extracted-model advantage. Factor ablation uses a fixed-probe necessity protocol; it measures what the current model uses, not whether task performance could be recovered after retraining without a given factor.

5 Conclusion

We discovered a compact hematopoietic manifold in scGPT, validated it on external datasets in strict zero-shot mode, and extracted it as a standalone algorithm that significantly outperforms established methods on pseudotime-depth alignment while remaining competitive on classification. Multi-stage compaction reduced the operator to a single attention head (5.9 MB) without significant loss, and further to a rank-64 surrogate (0.73 MB) whose four-factor mechanistic core resolves into explicit hematopoietic gene programs. To our knowledge, this represents the first competitive, biologically useful algorithm extracted from a foundation model via mechanistic interpretability, and the most detailed mechanistic decomposition of such an extracted algorithm. The extraction method generalizes to a second biological manifold family (intercellular communication) and is applicable to other foundation models and developmental systems.

References

- [1] M. Ashburner, C. A. Ball, J. A. Blake, D. Botstein, H. Butler, J. M. Cherry, A. P. Davis, K. Dolinski, S. S. Dwight, J. T. Eppig, M. A. Harris, D. P. Hill, L. Issel-Tarver, A. Kasarskis, S. Lewis, J. C. Matese, J. E. Richardson, M. Ringwald, G. M. Rubin, and G. Sherlock. Gene Ontology: tool for the unification of biology. *Nature Genetics*, 25(1):25–29, 2000.
- [2] Y. Belinkov and J. Glass. Analysis Methods in Neural Language Processing: A Survey. *Transactions of the Association for Computational Linguistics*, 7:49–72, 2019.
- [3] Y. Benjamini and Y. Hochberg. Controlling the False Discovery Rate: A Practical and Powerful Approach to Multiple Testing. *Journal of the Royal Statistical Society: Series B*, 57(1):289–300, 1995.
- [4] V. Bergen, M. Lange, S. Peidli, F. A. Wolf, and F. J. Theis. Generalizing RNA velocity to transient cell states through dynamical modeling. *Nature Biotechnology*, 38(12):1408–1414, 2020.
- [5] S. Bills, N. Cammarata, D. Mossing, H. Tillman, L. Gao, G. Goh, I. Sutskever, J. Leike, J. Wu, and W. Saunders. Language Models Can Explain Neurons in Language Models. OpenAI, 2023.
- [6] T. Bricken, A. Templeton, J. Batson, B. Chen, A. Jermyn, T. Conerly, N. L. Turner, C. Anil, C. Denison, A. Askell, R. Lasenby, Y. Wu, S. Kravec, N. Schiefer, T. Maxwell, N. Joseph, A. Tamkin, K. Nguyen, B. McLean, J. E. Burke, T. Hume, S. Carter, T. Henighan, and C. Olah. Towards Monosemanticity: Decomposing Language Models With Dictionary Learning. Anthropic, 2023.
- [7] K. Clark, U. Khandelwal, O. Levy, and C. D. Manning. What Does BERT Look At? An Analysis of BERT’s Attention. In *Proceedings of the BlackboxNLP Workshop, ACL*, 2019.
- [8] R. R. Coifman and S. Lafon. Diffusion maps. *Applied and Computational Harmonic Analysis*, 21(1):5–30, 2006.
- [9] A. Conmy, A. N. Mavor-Parker, A. Lynch, S. Heimersheim, and A. Garriga-Alonso. Towards Automated Circuit Discovery for Mechanistic Interpretability. In *Advances in Neural Information Processing Systems (NeurIPS)*, 2023.
- [10] H. Cui, C. Wang, H. Maan, K. Pang, F. Luo, N. Duan, and B. Wang. scGPT: Toward Building a Foundation Model for Single-Cell Multi-omics Using Generative AI. *Nature Methods*, 21(8):1470–1480, 2024.
- [11] C. Dominguez Conde, C. Xu, L. B. Jarvis, et al. Cross-tissue immune cell analysis reveals tissue-specific features in humans. *Science*, 376(6594):eabl5197, 2022.
- [12] N. Elhage, N. Nanda, C. Olsson, T. Henighan, N. Joseph, B. Mann, A. Askell, Y. Bai, A. Chen, T. Conerly, N. DasSarma, D. Drain, D. Ganguli, Z. Hatfield-Dodds, D. Hernandez, A. Jones, J. Kernion, L. Lovitt, K. Ndousse, D. Amodei, T. Brown, J. Clark, J. Kaplan, S. McCandlish, and C. Olah. A Mathematical Framework for Transformer Circuits. *Transformer Circuits Thread*, Anthropic, 2021.
- [13] N. Elhage, T. Hume, C. Olsson, N. Schiefer, T. Henighan, S. Kravec, Z. Hatfield-Dodds, R. Lasenby, D. Drain, C. Chen, R. Grosse, S. McCandlish, J. Kaplan, D. Amodei, M. Wattenberg, and C. Olah. Toy Models of Superposition. *Transformer Circuits Thread*, Anthropic, 2022.

- [14] J. Frankle and M. Carbin. The Lottery Ticket Hypothesis: Finding Sparse, Trainable Neural Networks. In *International Conference on Learning Representations (ICLR)*, 2019.
- [15] L. Garcia-Alonso, C. H. Holland, M. M. Ibrahim, D. Türei, and J. Saez-Rodriguez. Benchmark and integration of resources for the estimation of human transcription factor activities. *Genome Research*, 29(8):1363–1375, 2019.
- [16] A. Gayoso et al. Joint probabilistic modeling of single-cell multi-omic data with totalVI. *Nature Methods*, 18(3):272–282, 2021.
- [17] A. Geiger, H. Lu, T. Icard, and C. Potts. Causal Abstractions of Neural Networks. In *Advances in Neural Information Processing Systems (NeurIPS)*, 2021.
- [18] M. Geva, R. Schuster, J. Berant, and O. Levy. Transformer Feed-Forward Layers Are Key-Value Memories. In *Proceedings of the Conference on Empirical Methods in Natural Language Processing (EMNLP)*, 2021.
- [19] L. Haghverdi, M. Buttner, F. A. Wolf, F. Buettner, and F. J. Theis. Diffusion pseudotime robustly reconstructs lineage branching. *Nature Methods*, 13(10):845–848, 2016.
- [20] H. Han et al. TRRUST v2: an expanded reference database of human and mouse transcriptional regulatory interactions. *Nucleic Acids Research*, 46(D1):D380–D386, 2018.
- [21] M. Hao, J. Gong, X. Zeng, C. Liu, Y. Guo, X. Cheng, T. Wang, J. Ma, X. Zhang, and L. Song. Large-scale foundation model on single-cell transcriptomics. *Nature Methods*, 2024.
- [22] G. Hinton, O. Vinyals, and J. Dean. Distilling the Knowledge in a Neural Network. *arXiv preprint arXiv:1503.02531*, 2015.
- [23] J. Jumper, R. Evans, A. Pritzel, T. Green, M. Figurnov, O. Ronneberger, K. Tunyasuvunakool, R. Bates, A. Židek, A. Potapenko, A. Bridgland, C. Meyer, S. A. A. Kohl, A. J. Ballard, A. Cowie, B. Romera-Paredes, S. Nikolov, R. Jain, J. Adler, T. Back, S. Petersen, D. Reiman, E. Clancy, M. Zielinski, M. Steinegger, M. Pacholska, T. Berghammer, S. Bodenstein, D. Silver, O. Vinyals, A. W. Senior, K. Kavukcuoglu, P. Kohli, and D. Hassabis. Highly accurate protein structure prediction with AlphaFold. *Nature*, 596(7873):583–589, 2021.
- [24] I. Kendiukhov. Systematic evaluation of single-cell foundation model interpretability reveals attention captures co-expression rather than unique regulatory signal. *arXiv preprint arXiv:2602.17532*, 2026.
- [25] I. Kendiukhov. Causal circuit tracing reveals distinct computational architectures in single-cell foundation models: inhibitory dominance, biological coherence, and cross-model convergence. *arXiv preprint arXiv:2603.01752*, 2026.
- [26] I. Kendiukhov. Sparse autoencoders reveal organized biological knowledge but minimal regulatory logic in single-cell foundation models: a comparative atlas of Geneformer and scGPT. *arXiv preprint arXiv:2603.02952*, 2026.
- [27] I. Korsunsky, N. Millard, J. Fan, K. Slowikowski, F. Zhang, K. Wei, Y. Baglaenko, M. B. Brenner, P.-R. Loh, and S. Raychaudhuri. Fast, sensitive and accurate integration of single-cell data with Harmony. *Nature Methods*, 16(12):1289–1296, 2019.

- [28] G. La Manno, R. Soldatov, A. Zeisel, E. Braun, H. Hochgerner, V. Petukhov, K. Lidschreiber, M. E. Kastrioti, P. Lönnerberg, A. Furlan, J. Fan, L. E. Borm, Z. Liu, D. van Bruggen, J. Guo, X. He, R. Barker, E. Sundström, G. Castelo-Branco, P. Cramer, I. Adameyko, S. Linnarsson, and P. V. Kharchenko. RNA velocity of single cells. *Nature*, 560(7719):494–498, 2018.
- [29] E. Laurenti and B. Göttgens. From haematopoietic stem cells to complex differentiation landscapes. *Nature*, 553(7689):418–426, 2018.
- [30] Z. Lin et al. Evolutionary-scale prediction of atomic-level protein structure with a language model. *Science*, 379(6637):1123–1130, 2023.
- [31] R. Lopez, J. Regier, M. B. Cole, M. I. Jordan, and N. Yosef. Deep generative modeling for single-cell transcriptomics. *Nature Methods*, 15(12):1053–1058, 2018.
- [32] M. Lotfollahi, M. Naghipourfar, M. D. Luecken, M. Khajavi, M. Büttner, M. Wagenstetter, Z. Avsec, A. Gayoso, N. Yosef, M. Interlandi, S. Rybakov, A. V. Misharin, and F. J. Theis. Mapping single-cell data to reference atlases by transfer learning. *Nature Biotechnology*, 40(1):121–130, 2022.
- [33] C. Lu, C. Lu, R. T. Lange, J. Foerster, J. Clune, and D. Ha. The AI Scientist: Towards Fully Automated Open-Ended Scientific Discovery. *arXiv preprint arXiv:2408.06292*, 2024.
- [34] M. D. Luecken, M. Büttner, K. Chaichoompu, A. Danese, M. Interlandi, M. F. Mueller, D. C. Strobl, L. Zappia, M. Dugas, M. Colomé-Tatché, and F. J. Theis. Benchmarking atlas-level data integration in single-cell genomics. *Nature Methods*, 19(1):41–50, 2022.
- [35] S. Marks, C. Rager, E. J. Michaud, Y. Belinkov, D. Bau, and A. Mueller. Sparse Feature Circuits: Discovering and Editing Interpretable Causal Graphs in Language Models. *arXiv preprint arXiv:2403.19647*, 2024.
- [36] L. McInnes, J. Healy, and J. Melville. UMAP: Uniform manifold approximation and projection for dimension reduction. *arXiv preprint arXiv:1802.03426*, 2018.
- [37] K. Meng, D. Bau, A. Andonian, and Y. Belinkov. Locating and Editing Factual Associations in GPT. In *Advances in Neural Information Processing Systems (NeurIPS)*, 2022.
- [38] K. R. Moon et al. Visualizing structure and transitions in high-dimensional biological data. *Nature Biotechnology*, 37(12):1482–1492, 2019.
- [39] N. Nanda, L. Chan, T. Lieberum, J. Smith, and J. Steinhardt. Progress Measures for Grokking Via Mechanistic Interpretability. In *International Conference on Learning Representations (ICLR)*, 2023.
- [40] E. Nguyen, M. Poli, M. G. Durrant, B. Kang, D. Katrekar, D. B. Li, L. J. Bartie, A. W. Thomas, S. H. King, G. Brixi, J. Sullivan, M. Y. Ng, A. Lewis, A. Lou, S. Ermon, S. A. Baccus, T. Hernandez-Boussard, C. Ré, P. D. Hsu, and B. L. Hie. Sequence modeling and design from molecular to genome scale with Evo. *Science*, 386(6723):ead09336, 2024.
- [41] C. Olah, N. Cammarata, L. Schubert, G. Goh, M. Petrov, and S. Carter. Zoom In: An Introduction to Circuits. *Distill*, 5(3):e00024.001, 2020.
- [42] S. H. Orkin and L. I. Zon. Hematopoiesis: An Evolving Paradigm for Stem Cell Biology. *Cell*, 132(4):631–644, 2008.

- [43] K. Park, Y. J. Choe, and V. Veitch. The Linear Representation Hypothesis and the Geometry of Large Language Models. In *International Conference on Machine Learning (ICML)*, 2024.
- [44] F. Paul, Y. Arkin, A. Giladi, D. A. Jaitin, E. Kenigsberg, H. Keren-Shaul, D. Winter, D. Lara-Astiaso, M. Gury, A. Weiner, E. David, N. Cohen, F. K. B. Lauridsen, S. Haas, A. Schlitzer, A. Mildner, F. Ginhoux, S. Jung, A. Trumpp, B. T. Porse, A. Tanay, and I. Amit. Transcriptional Heterogeneity and Lineage Commitment in Myeloid Progenitors. *Cell*, 163(7):1663–1677, 2015.
- [45] M. Pearce, E. Simon, M. Byun, and D. Balsam. Finding the Tree of Life in Evo 2. Goodfire Research, <https://www.goodfire.ai/research/phylogeny-manifold>, 2025.
- [46] X. Qiu et al. Reversed graph embedding resolves complex single-cell trajectories. *Nature Methods*, 14(10):979–982, 2017.
- [47] A. Regev, S. A. Teichmann, E. S. Lander, I. Amit, C. Benoist, E. Birney, B. Bodenmiller, P. Campbell, P. Carninci, M. Clatworthy, H. Clevers, B. Deplancke, I. Dunham, J. Eberwine, R. Eils, W. Enard, A. Farmer, L. Fugger, B. Göttgens, N. Hacohen, M. Haniffa, M. Hemberg, S. Kim, P. Klenerman, A. Kriegstein, E. Lein, S. Linnarsson, E. Lundberg, J. Lundeberg, P. Majumder, J. C. Marioni, M. Merad, M. Mhlanga, M. Nawijn, M. Netea, G. Nolan, D. Pe’er, A. Phillipakis, C. P. Ponting, S. Quake, W. Reik, O. Rozenblatt-Rosen, J. Sanes, R. Satija, T. N. Schumacher, A. Shalek, E. Shapiro, P. Sharma, J. W. Shin, O. Stegle, M. Stratton, M. J. T. Stubbington, F. J. Theis, M. Uhlen, A. van Oudenaarden, A. Wagner, F. Watt, J. Weissman, B. Wold, R. Xavier, and N. Yosef. The Human Cell Atlas. *eLife*, 6:e27041, 2017.
- [48] A. Rives et al. Biological structure and function emerge from scaling unsupervised learning to 250 million protein sequences. *Proceedings of the National Academy of Sciences*, 118(15):e2016239118, 2021.
- [49] Y. Rosen, Y. Roohani, A. Agrawal, L. Samotorčan, Tabula Sapiens Consortium, S. R. Quake, and J. Leskovec. Universal Cell Embeddings: A Foundation Model for Cell Biology. *bioRxiv*, 2023.
- [50] S. T. Roweis and L. K. Saul. Nonlinear Dimensionality Reduction by Locally Linear Embedding. *Science*, 290(5500):2323–2326, 2000.
- [51] W. Saelens, R. Cannoodt, H. Todorov, and Y. Saeys. A comparison of single-cell trajectory inference methods. *Nature Biotechnology*, 37(5):547–554, 2019.
- [52] M. Setty, V. Kiseliovas, J. Levine, A. Gayoso, L. Mazutis, and D. Pe’er. Characterization of cell fate probabilities in single-cell data with Palantir. *Nature Biotechnology*, 37(4):451–460, 2019.
- [53] K. Street et al. Slingshot: cell lineage and pseudotime inference for single-cell transcriptomics. *BMC Genomics*, 19:477, 2018.
- [54] T. Stuart, A. Butler, P. Hoffman, C. Hafemeister, E. Papalexi, W. M. Mauck, Y. Hao, M. Stoeckius, P. Smibert, and R. Satija. Comprehensive Integration of Single-Cell Data. *Cell*, 177(7):1888–1902, 2019.
- [55] The Tabula Sapiens Consortium. The Tabula Sapiens: A multiple-organ, single-cell transcriptomic atlas of humans. *Science*, 376(6594):eabl4896, 2022.

- [56] A. Templeton, T. Conerly, J. Marcus, J. Lindsey, T. Bricken, B. Chen, A. Pearce, C. Citro, E. Ameisen, A. Jones, H. Cunningham, N. L. Turner, C. McDougall, M. MacDiarmid, A. Tamkin, E. Durmus, T. Hume, F. Mosconi, C. D. Freeman, T. R. Sumers, E. Rees, J. Batson, A. Jermyn, S. Carter, C. Olah, and T. Henighan. Scaling Monosemanticity: Extracting Interpretable Features from Claude 3 Sonnet. *Anthropic*, 2024.
- [57] J. B. Tenenbaum, V. de Silva, and J. C. Langford. A global geometric framework for nonlinear dimensionality reduction. *Science*, 290(5500):2319–2323, 2000.
- [58] V. G. Theodoris et al. Transfer learning enables predictions in network biology. *Nature*, 618(7965):616–624, 2023.
- [59] V. A. Traag, L. Waltman, and N. J. van Eck. From Louvain to Leiden: guaranteeing well-connected communities. *Scientific Reports*, 9:5233, 2019.
- [60] C. Trapnell et al. The dynamics and regulators of cell fate decisions are revealed by pseudotemporal ordering of single cells. *Nature Biotechnology*, 32(4):381–386, 2014.
- [61] D. Türei, A. Valdeolivas, L. Gul, N. Palacio-Escat, M. Klein, O. Ivanova, M. Olbei, A. Gábor, F. J. Theis, D. Modos, T. Korcsmáros, and J. Saez-Rodriguez. Integrated intra- and intercellular signaling knowledge for multicellular omics analysis. *Molecular Systems Biology*, 17(3):e9923, 2021.
- [62] A. Vaswani, N. Shazeer, N. Parmar, J. Uszkoreit, L. Jones, A. N. Gomez, L. Kaiser, and I. Polosukhin. Attention Is All You Need. In *Advances in Neural Information Processing Systems (NeurIPS)*, pages 5998–6008, 2017.
- [63] L. Velten, S. F. Haas, S. Raffel, S. Blaszkiwicz, S. Islam, B. P. Hennig, C. Hirche, C. Lutz, E. C. Buss, D. Nowak, T. Boch, W.-K. Hofmann, A. D. Ho, W. Huber, A. Trumpp, M. A. G. Essers, and L. M. Steinmetz. Human haematopoietic stem cell lineage commitment is a continuous process. *Nature Cell Biology*, 19(4):271–281, 2017.
- [64] J. Venna and S. Kaski. Local multidimensional scaling. *Neural Networks*, 19(6–7):889–899, 2006.
- [65] J. Vig, A. Madani, L. R. Varshney, C. Xiong, R. Socher, and N. F. Rajani. BERTology Meets Biology: Interpreting Attention in Protein Language Models. In *International Conference on Learning Representations (ICLR)*, 2021.
- [66] K. Wang, A. Variengien, A. Conmy, B. Shlegeris, and J. Steinhardt. Interpretability in the Wild: a Circuit for Indirect Object Identification in GPT-2 Small. In *International Conference on Learning Representations (ICLR)*, 2023.
- [67] C. Weinreb, A. Rodriguez-Fraticelli, F. D. Camargo, and A. M. Klein. Lineage tracing on transcriptional landscapes links state to fate during differentiation. *Science*, 367(6479):eaaw3381, 2020.
- [68] F. A. Wolf, P. Angerer, and F. J. Theis. SCANPY: large-scale single-cell gene expression data analysis. *Genome Biology*, 19:15, 2018.
- [69] F. A. Wolf et al. PAGA: graph abstraction reconciles clustering with trajectory inference through a topology preserving map of single cells. *Genome Biology*, 20:59, 2019.

- [70] F. Yang, W. Wang, F. Wang, Y. Fang, D. Tang, J. Huang, H. Lu, and J. Yao. scBERT as a large-scale pretrained deep language model for cell type annotation of single-cell RNA-seq data. *Nature Machine Intelligence*, 4:852–866, 2022.

Supplementary Material

S1. Autonomous research loop and hypothesis space

The project used an autonomous multi-role loop centered on executor and reviewer/critic roles, with explicit hypothesis selection, gate auditing, and fast pivot rules. This main paper focuses on the validated hematopoiesis branch (H65) and its closure tests; a second validated branch (H38) is reported in the Supplementary Material after these sections, while other non-passing branches are included only as condensed context. The autonomous loop followed three stages under fixed gates. First, multiple exploratory branches were rejected because they failed effect-size or holdout robustness criteria. Second, H65 emerged as the first strong positive branch, while its paired null branch (H66) remained non-passing. Third, closure analyses (subspace/objective gap-fill, ablation+CI tests, equation-level LET replication, and strict external non-overlap transfer) elevated the H65 line to a closed, high-confidence result. Detailed iteration-by-iteration logs remain in `iterations/` in the project repo.

S2. Artifact-closure protocol

Before interpreting any result, the loop enforced an artifact-closure pipeline:

- **A: local path reconciliation** (canonical-path verification),
- **B: local materialization** (rebuild missing derived artifacts),
- **C: network retrieval** (autonomous download when local recovery fails),
- **D: schema enrichment** (metadata audit and harmonization).

For the final H65 cycle, A and D succeeded, B/C were not required, and no unresolved artifacts remained.

S3. Equation-level LET objective details

The main text presents the core LET objective equations (Section 2.3). Here we document the shared quality gates applied across all panels:

- trustworthiness ≥ 0.80 ,
- random holdout corr ≥ 0.20 ,
- donor holdout corr ≥ 0.20 ,
- clade/branch holdout corr ≥ 0.20 .

These thresholds were fixed before any panel-specific evaluation and applied uniformly to internal, lung external, strict non-overlap external, and frozen zero-shot transfer panels. Positive claims were accepted only when all primary gates passed simultaneously.

S4. Frozen-head zero-shot transfer protocol

For the transfer confirmation run, we used a strict **train-once, transfer-many** protocol:

1. Train the LET head only on the internal H65 anchor panel and select the best internal dimension ($d = 10$).
2. Reconstruct that exact head deterministically (model seed 15052); freeze all parameters.
3. Build external anchors and sampled-cell views from a separate multi-donor immune panel (7 cohorts).
4. Apply the frozen head directly (zero-shot; no external optimization/retraining).
5. Evaluate alignment with the same blocked-permutation and trustworthiness controls.

This protocol separates representation transfer from dataset-specific fitting, which is important for future applications.

S5. Cell-trained transferable head variant

To test whether training granularity changes what the transferred manifold emphasizes, we trained an alternative internal head on individual cells (not anchors) and then transferred it zero-shot to the same strict non-overlap external anchors. The internal training set contained 6,925 mapped cells across 34 stages and 23 donors. We used a stage-balanced sampler (maximum 500 cells/stage) and optimized a weighted objective with four terms: stage-distance fitting, local-neighborhood preservation, reconstruction, and stage classification ($w_{\text{stage}} = 1.0$, $w_{\text{local}} = 0.1$, $w_{\text{recon}} = 0.08$, $w_{\text{cls}} = 0.4$; 120 epochs; batch size 896; $d = 10$). No external rows were used during head training and no external fine-tuning was allowed at evaluation time.

S6. Hybrid topology-preserving variant

We tested a hybrid head that augments the cell-level objective with an anchor-topology prior derived from the internal anchor LET-10D manifold. Let $\mu_s(z)$ be the latent centroid for stage s , and D_{ref} the pairwise stage-centroid distance matrix from the internal anchor head (shared stages only). The hybrid objective is:

$$\mathcal{L}_{\text{hybrid}} = \mathcal{L}_{\text{cell}} + \lambda_{\text{topo}} \|D(\mu(z)) - D_{\text{ref}}\|^2 + \lambda_{\text{compact}} \sum_s \mathbb{E}_{i \in s} \|z_i - \mu_s(z)\|^2.$$

We ran two sweeps on the same strict non-overlap external evaluation panel:

- **strong-topology sweep:** $\lambda_{\text{topo}} \in \{0.04, 0.08, 0.12, 0.18\}$, $\lambda_{\text{compact}} = 0.015$,
- **conservative sweep:** $\lambda_{\text{topo}} \in \{0.005, 0.01, 0.02, 0.03\}$, $\lambda_{\text{compact}} = 0$.

To choose a representative hybrid per sweep, we used a fixed external objective:

$$\text{score} = \rho_{\text{resid}} + 0.25 \text{AUC}_{\text{CD4/CD8}} + 0.25 \text{AUC}_{\text{Mono/Macro}} + 0.40 \text{silhouette}_{\text{branch}} - 0.20 \text{spread}_{\text{norm}}.$$

S7. Statistical controls and robustness tests

We applied donor/tissue blocked permutations, confound-residualized correlations, branch holdouts, objective ablations, and bootstrap confidence intervals. Positive claims were accepted only when all primary gates passed. Bootstrap estimates were stable across core endpoints: CD4/CD8 AUC mean 0.826, 95% CI [0.772, 0.876]; branch silhouette mean 0.404, 95% CI [0.362, 0.442]; residual ripple R^2 (PC4) mean 0.274, 95% CI [0.198, 0.344]. Across five seeds ($\{42, 43, 44, 45, 46\}$), trustworthiness remained high (0.979 ± 0.005), while CD4/CD8 AUC varied moderately (0.758 ± 0.013).

S8. Benchmark evaluation protocol details

To quantify practical utility of extracted heads, we ran donor-level post-hoc benchmarks on the strict non-overlap external panel (616 anchors, 21 donors). The finalized Robust-V2 campaign used grouped donor-holdout splits with 100,000 training cells per split and strict test-only evaluation. It comprises three completed batches: one full 40-split run (all methods including scVI) and two additional 24-split core-only runs, for 88 pooled splits total.

We compared paper-referenced extracted variants (anchor head, cell head, hybrid-conservative head) against raw-expression, PCA/SVD, CellTypist, scVI-10D, Scanpy-DPT, and Palantir baselines. Metrics were branch and stage macro-F1 / balanced accuracy, CD4/CD8 and monocyte/macrophage AUROC / balanced accuracy, and pseudotime-depth Spearman correlation.

As a targeted ablation, we also compared learned heads against two native frozen scGPT embedding baselines: (i) whole-human average-pooled contextual token embeddings and (ii) continual-pretrained `<cls>` embeddings.

Classification endpoints were evaluated strictly on held-out test donors for all methods. For pseudotime, all methods were evaluated with a donor-local test-only protocol (pseudotime was computed separately within each test donor’s cells), including donor-local native DPT/Palantir computation. We report both the primary signed pseudotime-depth Spearman and an orientation-aware summary (absolute Spearman and sign-share) to separate ordering strength from direction choice. Paired statistical comparisons were computed on split-level donor-mean differences using two-sided Wilcoxon signed-rank tests with BH-FDR correction.

S9. T-cell resolution lens methods

A key interpretability issue was apparent CD4/CD8 mixing in default 3D projections. We tested whether this reflected absent signal or projection loss. Using strict non-overlap external anchors, we compared separability in displayed 3D versus full 10D LET latent space. We then defined a visualization-only lens: keep global x/y , replace z by a discriminative latent-axis score (best CD4/CD8 dimension), preserving global context while exposing subtype separation.

S10. Flatness and ripple test methods

To test whether our geometry resembles the Goodfire “flat + ripples” pattern, we ran two related analyses.

Projection-level test (3D coordinates). For each 3D manifold view, we fit a best 2D plane (weighted PCA), quantified residual structure (Moran’s I on plane residuals), and scanned sinusoidal fits after quadratic detrending, with permutation tests.

Latent-level test (LET-10D coordinates). We reconstructed the exact LET-10D latent z , defined a 2D substrate using latent PC1/PC2, then for each residual axis (PC3–PC10) tested de-

trended sinusoidal structure over in-plane directions with permutation tests and BH-FDR correction across residual axes.

We used a conservative residual-axis significance rule ($q \leq 0.05$, sinusoid $R^2 \geq 0.10$, cycles-per-span ≥ 1.5). We additionally ran a covariance-matched Gaussian null calibration to verify that the detector does not trigger on generic anisotropic clouds.

S11. Phase-2 deepening protocol

To strengthen mechanistic interpretation beyond alignment and transfer, we ran a targeted second-pass protocol on the same H65 manifold:

- **Latent interventions:** move source anchors along biologically motivated latent directions (stem→erythroid, stem→myeloid, CD4→CD8), decode to feature space, and quantify monotonic target-fraction and graph-depth shifts.
- **Branchpoint quantification:** build stage-centroid kNN graphs, extract MST topology, and quantify root articulation, branchpoint count, endpoint reachability, and first-hop diversity from HSC.
- **Ripple semantics:** test whether significant residual ripple axes associate with curated biological program scores (Spearman + BH-FDR), then measure ripple R^2 change after program residualization.
- **Stability envelope:** bootstrap confidence intervals for key outcomes (CD4/CD8 AUC, branch silhouette, residual ripple R^2) and seed-sensitivity audits across $\{42, 43, 44, 45, 46\}$.

S12. Extraction pipeline terminology and compression stages

Because later compression experiments build on the same exported object, we make the pipeline boundary explicit. The reported standalone method has three stages:

1. **Direct operator extraction from scGPT.** Starting from the frozen whole-human checkpoint, we read native attention operators $A_{\ell,h} \in \mathbb{R}^{1200 \times 1200}$ and construct a fixed feature map. This stage is a direct checkpoint export: no target labels are used and no parameters are optimized.
2. **Small learned adaptor on top of the extracted operator.** We train a lightweight head g_θ on internal data only, mapping fixed extracted features to the task-agnostic manifold latent z (typically $d = 10$). This is the only learned part of the shared representation.
3. **Task-specific readout.** For downstream classification or regression, we train a separate probe h_ϕ on top of z . These probes are deliberately small and are not part of the extracted representation itself.

Thus, the benchmarked representation should be described precisely as *directly extracted scGPT operator + small learned adaptor*, not as a zero-learning export of the entire pipeline.

This distinction governs later compression stages. Compact-V1 remains a *directly extracted operator* because it replaces the pooled drift map by a weighted sum of native top-ranked heads,

$$\tilde{A}_k = \sum_{i=1}^k \alpha_i A_{\ell_i, h_i},$$

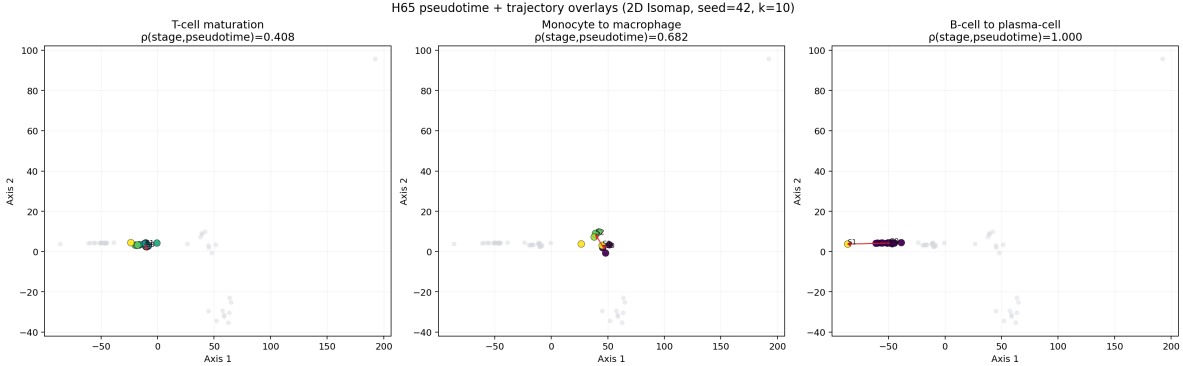


Figure 6: Pseudotime-annotated manifold view used for trajectory interpretation. The projection emphasizes developmental ordering from stem/progenitor regions toward branch-specific lineage endpoints.

while still retraining only the small adaptor and downstream probe. By contrast, any subsequent low-rank, sparse, or quantized compression of \tilde{A}_k should be interpreted as a *compressed surrogate of the extracted operator*, not as a direct checkpoint export of new native scGPT parameters.

In the low-rank compression step, we fit truncated-SVD surrogates

$$\tilde{A}_k \approx U_r V_r^\top, \quad r \in \{8, 16, 32, 64\},$$

for the compact top1/top2 operators and then retrain only the same lightweight 10D adaptor and downstream task probes. In the sparse follow-up, we applied a hard top- k pruning rule to the selected rank64 surrogate: retain only a subset of parent factors and keep only the top- k read genes and top- k write genes per retained factor. This produces an even smaller *sparse surrogate of the low-rank surrogate*, again followed by retraining only the same adaptor and downstream probes.

For the factor-necessity audit, we took the selected rank64 surrogate and kept its downstream task probes fixed. Each leave-one-out ablation zeroed a single factor only at inference time while leaving all other factors and the trained probes unchanged. This fixed-probe protocol measures *necessity of the existing factorization*, not recoverability after retraining; retraining after each factor drop would answer a different question.

S13. Trajectory and stage-order consistency

Trajectory analyses support developmental ordering for several hematopoietic paths. In the expanded manifold, strongest significant signals were erythroid $\rho = 0.768, p = 0.0017$, granulocytic $\rho = 0.568, p = 0.0033$, and trunk HSC/HPC/CMP $\rho = 0.611, p = 0.0183$. A coarse canonical myeloid trajectory remained positively associated ($\rho = 0.682, p = 0.026$), while fine monocyte→macrophage ordering in the expanded panel was weak/non-significant ($\rho = 0.082, p = 0.238$). B→plasma ordering was monotonic but small-sample limited (high ρ , non-significant p in current anchor counts).

S14. Methodological closure and effective dimensionality

Flat-subspace training confirmation. We verified that training the adaptor head in a flat (linear) subspace also passes transfer gates. The best flat-subspace dimension was $d = 8$, with random/donor/clade holdout correlation means of 0.609/0.647/0.316. The T/NK branch remained the weakest transfer target across all tested configurations.

Table 8: Anchor-trained vs cell-trained head on the same strict non-overlap external panel (global 3D view unless noted).

Metric	Anchor-trained	Cell-trained
Corr (projected distance vs target)	0.607	0.614
Residualized corr	0.605	0.612
Trustworthiness	0.972	0.969
CD4/CD8 AUC(abs), global 3D	0.744	0.886
Monocyte/Macrophage AUC(abs), global 3D	0.759	0.937
Normalized within-stage spread	0.217	0.314
Branch silhouette mean (3D)	0.013	0.008
Stem→(plasma minus B-cell) distance	+95.740	−3.844

Objective and confidence-interval closure. The best ablation configuration (combined distance and reconstruction objective at $d = 3$) achieved random/donor/tissue/clade holdout means of 0.637/0.610/0.571/0.301, with bootstrap confidence intervals reported for each axis and improved T/NK transfer relative to the prior baseline.

Effective dimensionality. A three-dimensional projection is a visualization slice rather than the full manifold. In strict external non-overlap LET transfer, the selection objective increased consistently with dimensionality:

- $d = 3$: objective 0.507, trustworthiness 0.946,
- $d = 6$: objective 0.604, trustworthiness 0.976,
- $d = 10$: objective 0.632, trustworthiness 0.985,

with all holdout gates passing at each tested d . In explicit flat-subspace training, the best objective was at $d = 8$ (objective 0.475). Together these results support an effective hematopoietic manifold size of approximately 8–10 dimensions.

Internal LET confirmation. The internal latent embedding transfer fully passed all quality gates (Table 1), confirming that the transfer protocol is consistent between internal and external panels.

S15. Anchor-trained versus cell-trained head comparison

Using the same strict non-overlap external anchor panel (616 anchors), we compared the original anchor-trained transferable head with the cell-trained transferable head (Table 8). The cell-trained head slightly improved alignment metrics (corr 0.607 \rightarrow 0.614, residualized corr 0.605 \rightarrow 0.612) and strongly improved global 3D subtype separability (CD4/CD8 AUC 0.744 \rightarrow 0.886, monocyte/macrophage AUC 0.759 \rightarrow 0.937). Trustworthiness remained high but decreased slightly (0.972 \rightarrow 0.969).

The tradeoff appears in global display geometry: normalized within-stage spread increased (0.217 \rightarrow 0.314), branch silhouette decreased (0.013 \rightarrow 0.008), and a stem-centric radial proxy changed sign (stem-to-plasma minus stem-to-B distance +95.740 \rightarrow −3.844). Cell-level training sharpens subtype margins but relaxes the compact branch-like arrangement seen in the anchor-trained map.

Table 9: Transfer-head tradeoff frontier on strict non-overlap external anchors (global 3D metrics).

Metric	Anchor-trained	Cell-trained	Hybrid strong-topology	Hybrid conservative
Corr	0.607	0.614	0.473	0.634
Residualized corr	0.605	0.612	0.472	0.632
Trustworthiness	0.972	0.969	0.969	0.959
CD4/CD8 AUC(abs), global 3D	0.744	0.886	0.934	0.911
Monocyte/Macrophage AUC(abs), global 3D	0.759	0.937	0.914	0.851
Normalized within-stage spread	0.217	0.314	0.348	0.318
Branch silhouette mean (3D)	0.013	0.008	0.102	0.037
Stem→(plasma minus B-cell) distance	+95.740	-3.844	+4.167	-0.397

Table 10: Robust-V2 pseudotime orientation summary across pooled donor rows. Signed ρ is the primary metric; $|\rho|$ and positive-sign share are orientation-aware summaries.

Method	n_{rows}	Mean signed ρ	Mean $ \rho $	Positive-share (%)
H65 anchor head (10D)	307	0.093	0.235	65.1
H65 cell head (10D)	352	0.249	0.439	71.0
H65 hybrid conservative (10D)	307	0.132	0.364	64.5
Raw baseline (1200 log1p)	307	-0.044	0.266	37.5
PCA-10 baseline	307	-0.007	0.259	38.1
SVD-10 baseline	307	0.002	0.279	51.8
CellTypist stage-probability baseline	306	-0.064	0.253	41.5
scVI-10D baseline	125	-0.103	0.274	37.6
Scanpy-DPT baseline	307	-0.089	0.261	34.9
Palantir baseline	275	-0.049	0.331	47.3

S16. Hybrid topology-preserving sweep

The hybrid runs defined a clear Pareto-like frontier between developmental branch readability and stage-distance alignment. In the **strong-topology sweep**, the best run ($\lambda_{\text{topo}} = 0.08$) produced the clearest branch geometry (branch silhouette 0.102; stem→(plasma minus B-cell) radial proxy +4.167), and retained strong subtype separation (CD4/CD8 AUC 0.934, monocyte/macrophage AUC 0.914). The tradeoff was reduced global alignment ($\text{corr}_{\text{resid}} = 0.472$).

In the **conservative sweep**, the best run ($\lambda_{\text{topo}} = 0.005$) preserved alignment (corr 0.634, $\text{corr}_{\text{resid}} = 0.632$) while keeping strong CD4/CD8 separability (0.911); monocyte/macrophage separability dropped relative to pure cell-trained transfer (0.851 vs 0.937), and topology gains were more modest (branch silhouette 0.037).

S17. Metric-level paired significance, orientation summary, and classification deltas

The orientation-aware view preserves the same ranking at the top: the cell head has both the highest signed mean and the highest absolute mean ($|\rho| = 0.439$). Several baselines show non-trivial absolute association (for example Palantir $|\rho| = 0.331$) but with weaker sign stability (positive-share near 35–52%), consistent with frequent orientation reversals across donor-local evaluations.

This pooled paired view confirms a mixed classification profile and a strong pseudotime profile. The cell head is significantly better than the strongest comparator on CD4/CD8 AUROC, CD4/CD8 balanced accuracy, mono/macro AUROC, and pseudotime-depth Spearman; branch balanced accuracy is numerically close and not significantly different at $\text{BH-}q \leq 0.05$. In contrast, branch

Table 11: Robust-V2 metric-level paired significance summary versus H65 cell head (comparator minus cell head; higher is better for all metrics).

Metric	Cell head mean	Best comparator (mean)	Mean diff	Wilcoxon BH- q
Branch balanced accuracy	0.828	Raw baseline (0.826)	-0.0018	1.5×10^{-1}
Branch macro-F1	0.584	Palantir baseline (0.621)	+0.0358	1.4×10^{-10}
Stage balanced accuracy	0.552	Raw baseline (0.567)	+0.0148	1.8×10^{-7}
Stage macro-F1	0.216	Palantir baseline (0.242)	+0.0254	1.3×10^{-6}
CD4/CD8 AUROC	0.867	H65 hybrid conservative (0.858)	-0.0088	1.1×10^{-15}
CD4/CD8 balanced accuracy	0.798	H65 hybrid conservative (0.794)	-0.0025	1.3×10^{-2}
Mono/Macro AUROC	0.951	H65 hybrid conservative (0.949)	-0.0014	7.1×10^{-3}
Mono/Macro balanced accuracy	0.864	PCA-10 baseline (0.871)	+0.0075	1.0×10^{-8}
Pseudotime-depth Spearman	0.249	H65 hybrid conservative (0.132)	-0.0561	2.7×10^{-7}

macro-F1, stage balanced accuracy, stage macro-F1, and mono/macro balanced accuracy are significantly led by specific baselines.

Sign interpretation note. Pseudotime-depth Spearman in Table 3 is the raw signed correlation $\rho = \text{Spearman}(\text{inferred pseudotime}, \text{ontology depth})$, not a baseline-normalized score. Positive values indicate alignment with increasing developmental depth; negative values indicate inverse ordering. Negative signed ρ does not necessarily imply absent trajectory signal, because pseudotime orientation can be reversed by root choice or manifold direction; Table 10 therefore reports orientation-aware summaries.

Scope closure and residual caveats in Robust V2. The prior scope mismatch for native diffusion pseudotime is closed: all methods were evaluated donor-locally on test-only cells. Residual limitations remain. Test donor count per split is fixed at 4, and donor reuse is substantial (15 unique test donors across 88 pooled splits; 14 unique donors in the strict 40-split full-method subset). Method coverage is uneven for some endpoints (pseudotime rows: Palantir 70 splits, scVI 36 splits). To stress fairness, we additionally inspected the strict 40-split full-method subset, where the same pseudotime ordering persisted (cell head 0.236, scVI -0.103 , all paired deltas negative).

S18. Unsupervised branch-inference benchmark

Because branch classification only tests label decodability, we added a separate branch-inference readout on the canonical 100k donor-holdout split (100k train, 139,357 test cells, 4 held-out donors). Each representation is passed to the same unsupervised branch wrapper without training a supervised branch classifier, and the resulting partitions are compared against annotation-derived reference branch groups.

On the full-coverage Scanpy-PAGA-Leiden benchmark, the raw-expression baseline is best on all four partition-agreement metrics, with the hybrid head close behind; the cell head is intermediate rather than dominant. This differs from the pseudotime benchmark, where the cell head is clearly best. The interpretation is that branch identity is highly decodable from the extracted head, but unsupervised coarse branch partition recovery is still strongest in raw or hybrid geometries under the current wrapper.

Palantir audit. The corrected Palantir branch-inference rerun evaluated the same held-out donors for all methods: {TSP10, TSP14, TSP17, TSP26}. However, valid Palantir outputs remained method-dependent because some donor/method pairs failed to produce at least two terminal states or encountered numerical errors. Table 14 lists the donor-level success matrix.

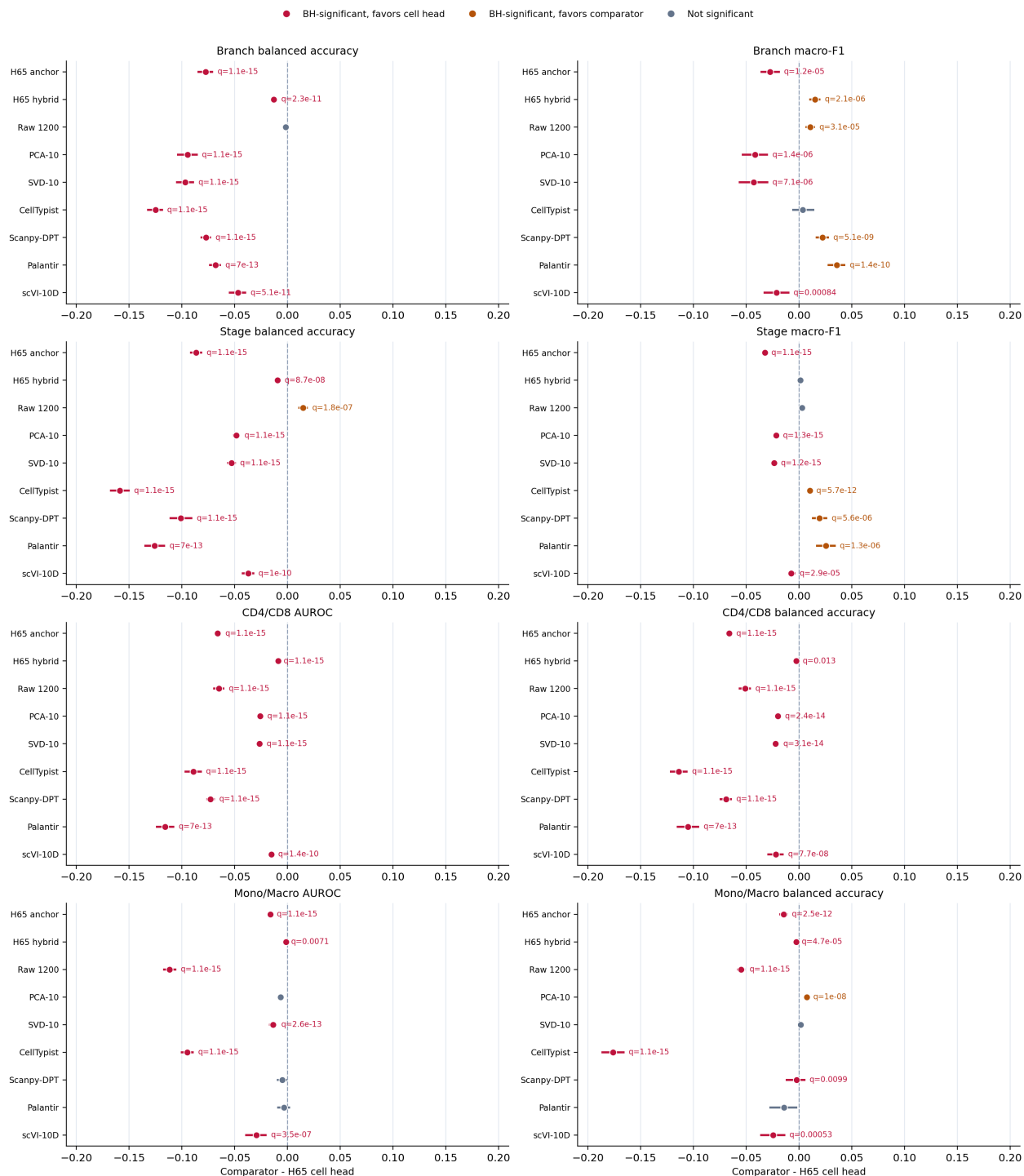


Figure 7: Robust-V2 splitwise paired deltas versus the H65 cell head for the eight non-pseudotime endpoints. Each panel shows comparator-minus-cell-head mean differences with 95% bootstrap confidence intervals across grouped donor-holdout splits. Negative values favor the cell head. Red points indicate BH-significant cell-head advantages; gold points indicate BH-significant comparator advantages.

Table 12: Canonical 100k split unsupervised branch-inference benchmark using Scanpy [68] neighbors+Leiden [59]+PAGA. Values are donor-level means across all 4 held-out donors.

Method	ARI	AMI	NMI	V-measure
H65 anchor head (10D)	0.269	0.546	0.547	0.547
H65 cell head (10D)	0.330	0.520	0.521	0.521
H65 hybrid conservative (10D)	0.387	0.618	0.619	0.619
Raw baseline (1200 log1p)	0.393	0.626	0.627	0.627
PCA-10 baseline	0.305	0.581	0.582	0.582
SVD-10 baseline	0.326	0.591	0.592	0.592
Frozen scGPT avg-pool	0.302	0.555	0.557	0.557
Frozen scGPT CP- <code><c1s></code>	0.315	0.574	0.576	0.576

Table 13: Canonical 100k split unsupervised branch-inference benchmark using Palantir fate assignments after a fair-scope rerun with frozen donor-local evaluation subsets and explicit audit logging.

Method	n_d	ARI	AMI	NMI	V-measure
H65 anchor head (10D)	2	0.613	0.670	0.670	0.670
H65 cell head (10D)	4	0.120	0.293	0.294	0.294
H65 hybrid conservative (10D)	3	0.255	0.410	0.410	0.410
Raw baseline (1200 log1p)	3	0.338	0.437	0.437	0.437
PCA-10 baseline	2	0.145	0.288	0.288	0.288
SVD-10 baseline	3	0.358	0.461	0.462	0.462
Frozen scGPT avg-pool	1	0.198	0.353	0.353	0.353
Frozen scGPT CP- <code><c1s></code>	2	0.300	0.334	0.335	0.335

Across the 32 Palantir donor/method jobs, 20 succeeded and 12 failed. Failures were dominated by “Palantir produced < 2 terminal states” (10 cases), with one infinity-bearing run and one eigensolver non-convergence. Because no donor succeeded for all methods simultaneously, the strict all-method shared-donor intersection was empty. We therefore treat Palantir as a qualitative stress test rather than a decisive ranking benchmark.

S19. Embedding ablation

To determine whether the extracted head adds value beyond what is already present in scGPT’s native embeddings, we compared it against two frozen scGPT embedding readouts: the average-pooled contextual embedding (averaging over all token positions) and the `<c1s>`-token embedding (a single summary vector from the model’s cell-processing checkpoint).

The cell-trained head outperforms both frozen embedding baselines on 6/7 metrics versus avg-pool and on all 7/7 versus CP-`<c1s>`. The largest gains are on subtype-sensitive endpoints (CD4/CD8



Figure 8: Supervised branch classification versus unsupervised branch recovery on the canonical 100k donor-holdout split. The task distinction is visible: branch information can be decodable under supervision even when unsupervised branch recovery remains wrapper- and coverage-sensitive.

Table 14: Palantir donor-level success matrix on the canonical 100k donor-holdout split.

Method	TSP10	TSP14	TSP17	TSP26
Raw baseline (1200 log1p)	ok	fail	ok	ok
PCA-10 baseline	ok	ok	fail	fail
SVD-10 baseline	ok	ok	fail	ok
Frozen scGPT avg-pool	fail	ok	fail	fail
Frozen scGPT CP-<cls>	fail	ok	fail	ok
H65 anchor head (10D)	ok	fail	ok	fail
H65 cell head (10D)	ok	ok	ok	ok
H65 hybrid conservative (10D)	ok	fail	ok	ok

and mono/macro AUROC) and stage-focused classification, while branch-level separability is already comparatively strong in native embeddings. Paired donor-level tests are directionally consistent but none survive BH-FDR ($q > 0.05$) because per-metric donor counts are small ($n_d = 2$ to 4). We therefore treat this as targeted supporting evidence.

S20. Stronger frozen-encoder baseline (4D and 10D comparisons)

4D extracted head versus frozen scGPT + MLP. To test a stronger direct-readout baseline under repeated-split statistics, we ran a grouped donor-holdout campaign with 12 splits comparing a 4D H65 cell head against frozen whole-human scGPT average-pooled embeddings with task-specific 3-layer MLP probes ($512 \rightarrow 256 \rightarrow 128 \rightarrow 64 \rightarrow C$, dropout 0.1).

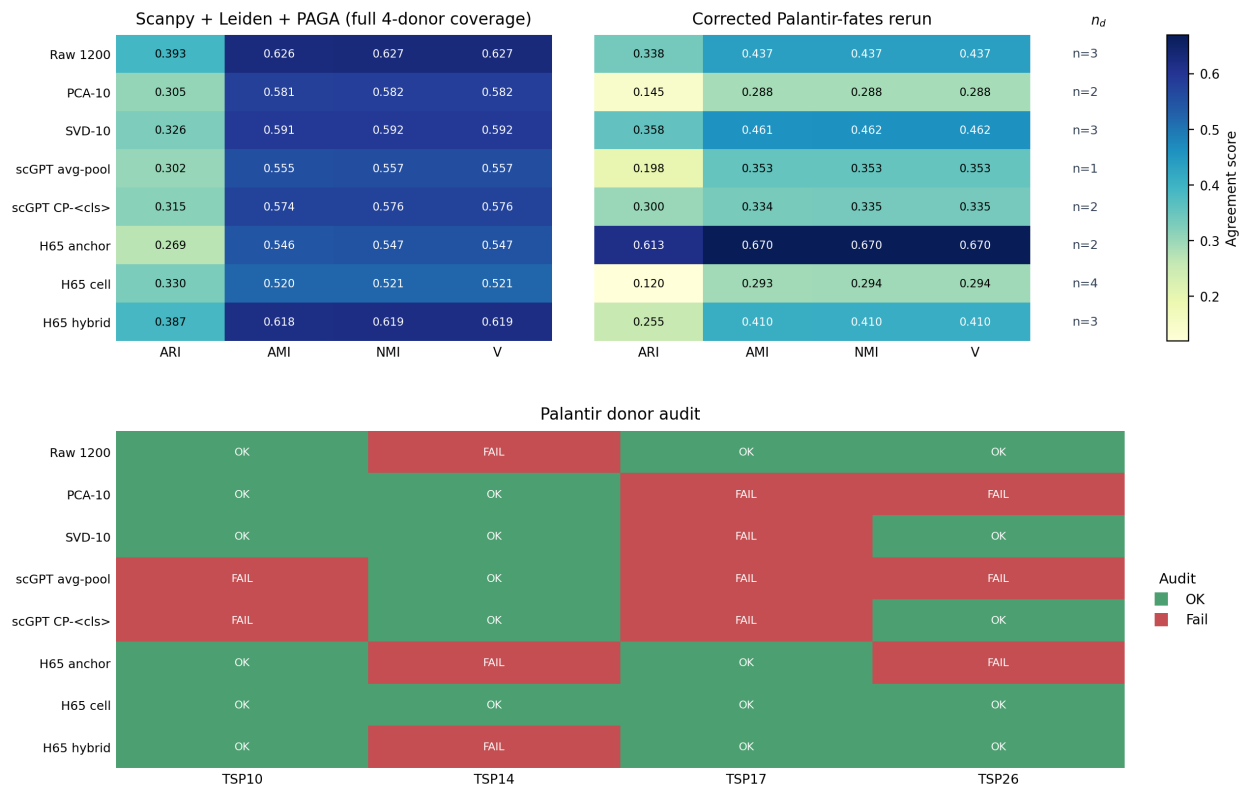


Figure 9: Branch-inference wrapper comparison. The Scanpy wrapper yields stable full-coverage rankings, whereas Palantir’s strongest mean scores are tied to reduced donor support.

Table 15: Embedding-ablation comparison on the held-out donor split (20k train, 30,137 test). Values are donor-level means.

Metric	H65 cell head (10D)	scGPT avg-pool	scGPT CP-<c1s>
Branch balanced accuracy ($n_d = 4$)	0.866	0.880	0.861
Branch macro-F1 ($n_d = 4$)	0.529	0.526	0.503
Stage balanced accuracy ($n_d = 4$)	0.610	0.593	0.570
Stage macro-F1 ($n_d = 4$)	0.188	0.154	0.145
CD4/CD8 AUROC ($n_d = 3$)	0.890	0.825	0.828
Mono/Macro AUROC ($n_d = 2$)	0.926	0.798	0.775
Pseudotime-depth Spearman ($n_d = 4$)	0.011	-0.071	-0.044

The 4D head improves pooled metrics on 7/8 endpoints, with 5/8 advantages remaining BH-significant after paired splitwise correction. This rules out the alternative explanation that the head only looked favorable when native embeddings were paired with simplistic linear probes.

10D extracted head + 2-layer MLP versus frozen scGPT + MLP. We then tightened the comparison using a 10D H65 cell head with a 2-layer task probe ($10 \rightarrow 64 \rightarrow C$).

The 10D+MLP2 variant exceeds the frozen-scGPT baseline on 7/8 pooled metrics with 6/8 BH-significant after paired splitwise correction.

Table 16: Repeated grouped-split comparison between a 4D extracted H65 cell head with linear probes and frozen scGPT avg-pool embeddings with 3-layer MLP probes ($n_{\text{split}} = 12$). Negative deltas favor the extracted head.

Metric	n_{obs}	H65 cell head (4D) + linear	Frozen scGPT avg-pool + MLP	$\Delta_{\text{base-head}}$	95% CI	BH- q
Branch macro-F1	40	0.597	0.547	-0.045	[-0.067, -0.023]	0.010
Branch balanced accuracy	40	0.801	0.810	0.010	[-0.001, 0.024]	0.192
Stage macro-F1	40	0.236	0.157	-0.078	[-0.087, -0.068]	0.0013
Stage balanced accuracy	40	0.540	0.403	-0.127	[-0.164, -0.086]	0.0020
CD4/CD8 AUROC	29	0.845	0.817	-0.026	[-0.033, -0.018]	0.0013
CD4/CD8 balanced accuracy	29	0.780	0.744	-0.034	[-0.045, -0.025]	0.0013
Mono/Macro AUROC	28	0.953	0.946	-0.005	[-0.014, 0.004]	0.279
Mono/Macro balanced accuracy	28	0.880	0.844	-0.034	[-0.069, -0.001]	0.119

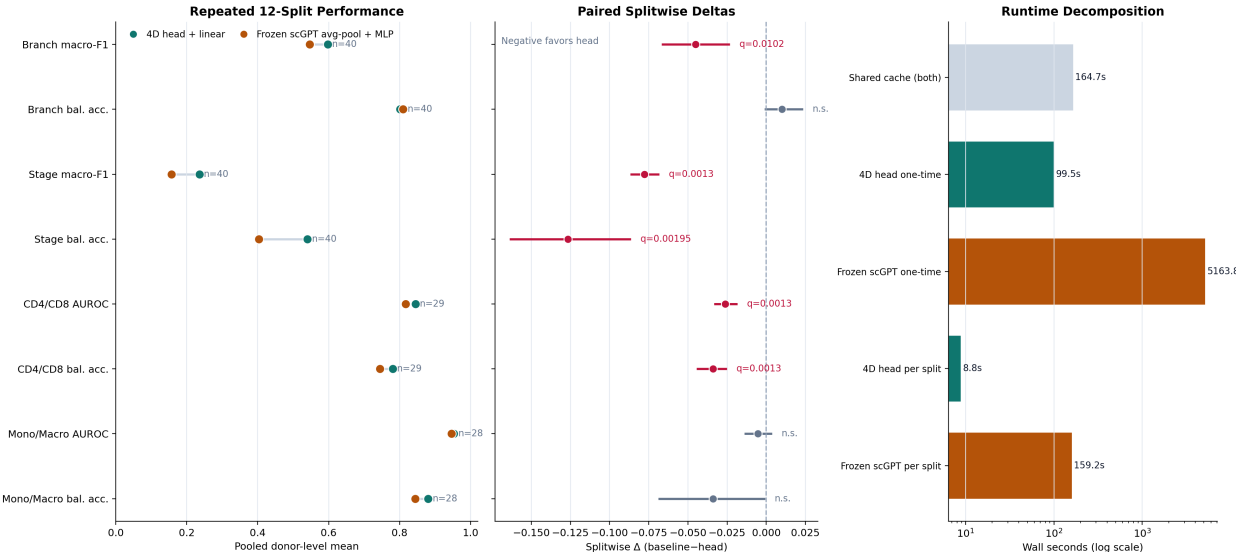


Figure 10: Repeated 12-split comparator between a 4D extracted head and frozen scGPT avg-pool embeddings with 3-layer MLP probes. Left: pooled means. Middle: paired splitwise deltas. Right: runtime decomposition.

S21. Probe-depth comparison

We closed the downstream probe-depth question on the broader 40-split Robust-V2 family. We evaluated the robust linear extracted head against both a modest non-linear readout (MLP2, $10 \rightarrow 64 \rightarrow C$) and a deeper alternative (MLP3, $10 \rightarrow 128 \rightarrow 64 \rightarrow C$). Neither nonlinear probe becomes the new default: MLP2 yields BH-significant gains on CD4/CD8 AUROC (+0.0045) and CD4/CD8 balanced accuracy (+0.0049), but significantly worsens mono/macro balanced accuracy (-0.0076) and both stage endpoints. We therefore keep the linear 10D head as the main robust classifier result, and treat MLP2 as the best targeted nonlinear follow-up when CD4/CD8 discrimination is the priority.

S22. Direct learnability baseline

To test whether a comparably small model trained directly on raw expression would recover the same task structure, we trained two direct raw-expression baselines on the same 12 grouped donor-holdout splits: a 1-hidden-layer model ($1200 \rightarrow 64 \rightarrow C$) and a 2-hidden-layer model ($1200 \rightarrow 128 \rightarrow 64 \rightarrow C$), both on $\log(1+x)$ input.

Table 17: Repeated grouped-split comparison between a 10D extracted H65 cell head with 2-layer MLP probes and frozen scGPT avg-pool + 3-layer MLP probes ($n_{\text{split}} = 12$). Positive deltas favor the extracted head.

Metric	n_{obs}	H65 cell head (10D) + MLP2	Frozen scGPT avg-pool + MLP	$\Delta_{\text{head-base}}$	95% CI	BH- q
Branch balanced accuracy	40	0.827	0.810	0.017	[0.012, 0.024]	0.0011
Branch macro-F1	40	0.556	0.547	0.010	[-0.003, 0.022]	0.194
Stage balanced accuracy	40	0.468	0.403	0.063	[0.048, 0.077]	0.0011
Stage macro-F1	40	0.180	0.157	0.024	[0.020, 0.027]	0.0011
CD4/CD8 AUROC	29	0.856	0.817	0.038	[0.032, 0.044]	0.0011
CD4/CD8 balanced accuracy	29	0.779	0.744	0.034	[0.028, 0.040]	0.0011
Mono/Macro AUROC	28	0.956	0.946	0.010	[0.004, 0.017]	0.031
Mono/Macro balanced accuracy	28	0.865	0.844	0.021	[0.002, 0.042]	0.124

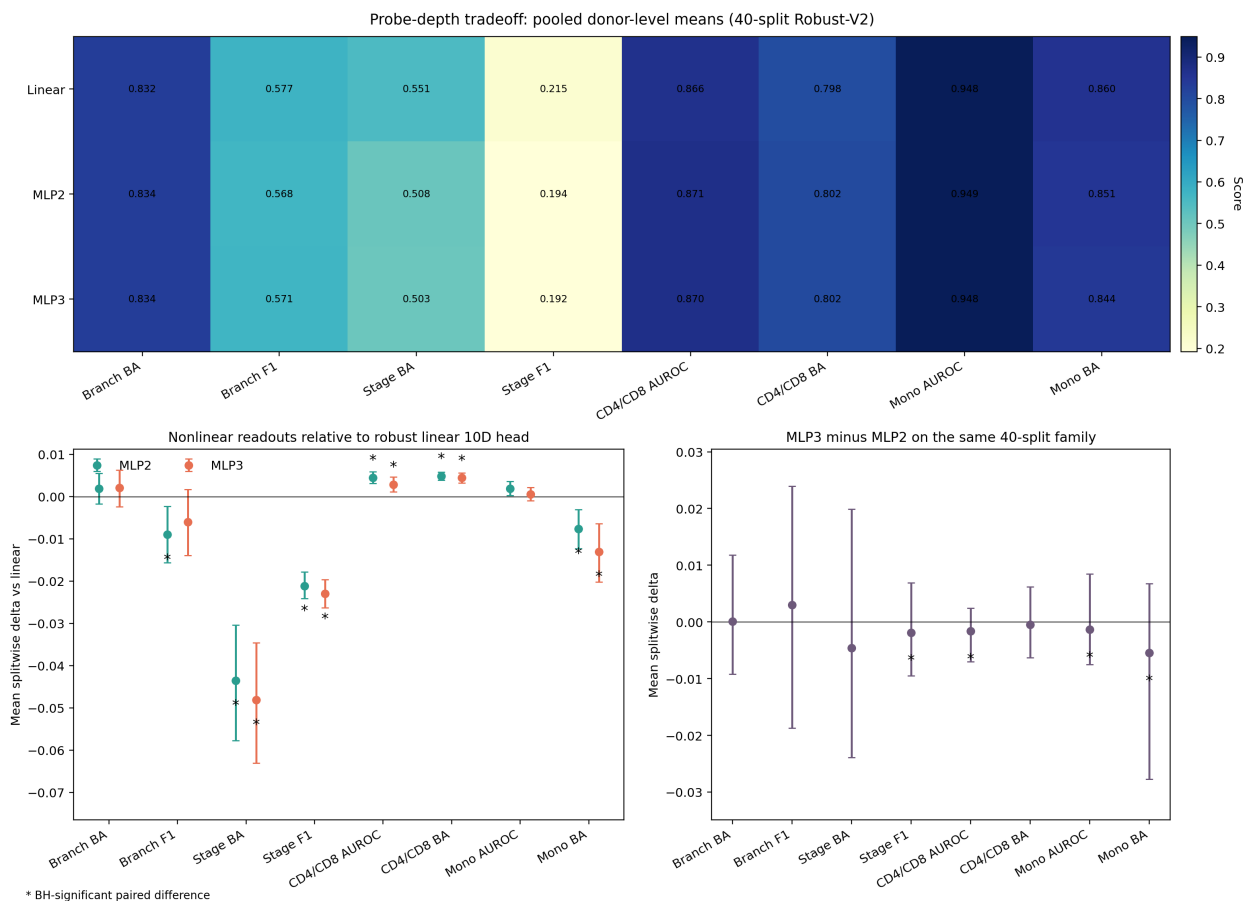


Figure 11: Probe-depth tradeoff for the extracted 10D H65 cell head on the 40-split Robust-V2 family. The linear head remains the best overall default.

Direct tiny models learn meaningful biology from raw expression, especially stage structure, but they do not recover the extracted head’s stronger subtype-sensitive geometry. Neither direct model dominates the extracted head: relative to the extracted 10D+MLP2, both direct models are significantly worse on CD4/CD8 AUROC, CD4/CD8 balanced accuracy, and mono/macro AUROC. The extraction result is not reducible to “just train a tiny MLP on raw input.”

Table 18: Repeated grouped-split comparison between direct tiny-from-scratch raw-expression MLPs, frozen scGPT avg-pool + MLP, and the extracted 10D head + MLP2. Values are pooled donor-level means across 12 splits.

Metric	Frozen scGPT + MLP	Direct raw1200 1 × 64	Direct raw1200 128 → 64	Extracted 10D + MLP2
Branch balanced accuracy	0.810	0.814	0.818	0.827
Branch macro-F1	0.547	0.550	0.557	0.556
Stage balanced accuracy	0.403	0.499	0.504	0.468
Stage macro-F1	0.157	0.190	0.186	0.180
CD4/CD8 AUROC	0.817	0.828	0.827	0.856
CD4/CD8 balanced accuracy	0.744	0.758	0.759	0.779
Mono/Macro AUROC	0.946	0.926	0.920	0.956
Mono/Macro balanced accuracy	0.844	0.866	0.863	0.865

Table 19: Runtime decomposition for the repeated-split 4D-head versus frozen scGPT+MLP comparator.

Component	Scope	H65 cell head (4D) + linear	Frozen scGPT avg-pool + MLP
Reference 1200-gene matrix extraction	one-time shared		164.7 s
Method-specific cache build	one-time	99.5 s (drift + head training)	5163.8 s (avg-pool extraction)
Per-split evaluation	mean / split	8.8 s	159.2 s
Trainable parameters / task	downstream	5–170	172,610–174,690

S23. Runtime comparison

The method-specific cache build is ~ 99.5 seconds for the extracted-head path versus ~ 5163.8 seconds for frozen scGPT avg-pool embeddings ($\sim 52\times$ gap). Per-split evaluation costs ~ 8.8 seconds for the head path versus ~ 159.2 seconds for the frozen-scGPT-MLP path ($\sim 18\times$ gap). Aggregated over the full 12-split campaign, the extracted-head path requires ~ 204.8 seconds versus ~ 7074.4 seconds for frozen scGPT ($\sim 34.5\times$ difference).

S24. T-cell resolution lens

Permutation tests confirmed that T-cell subtype information (CD4 versus CD8) is genuinely present in the extracted features, not an artifact of dimensionality (CD4-vs-CD8 AUROC 0.770, permutation $p = 0.005$; naive-vs-mature AUROC 0.752, permutation $p = 0.005$).

However, the default 3D visualization under-represents this signal: CD4-vs-CD8 AUROC is only 0.646 in the displayed 3D projection but 0.822 in the full 10D latent space, with the strongest single axis at dimension 4 (AUROC 0.845). To address this, we introduced a regularized enhancement that amplifies the most discriminative T-cell axis while preserving the global manifold structure. At the selected regularization strength ($\lambda = 8$), CD4-vs-CD8 AUROC improved from 0.835 to 0.901 with negligible loss in trustworthiness ($\Delta = 0.0018$).

This motivated the *T-cell separation lens*: a visualization tool that preserves the global manifold layout in the x/y plane while mapping the most discriminative T-cell axis to the z -coordinate. The lens improves interpretability of T-cell subtypes without changing the underlying quantitative metrics.

Dimension-wise functional interpretation. The first three latent dimensions are biologically meaningful but do not primarily encode CD4/CD8 separation:

- **dim 1:** broad branch axis with strong B/plasma loading (AUC 0.868); stage/branch η^2 0.895/0.869.

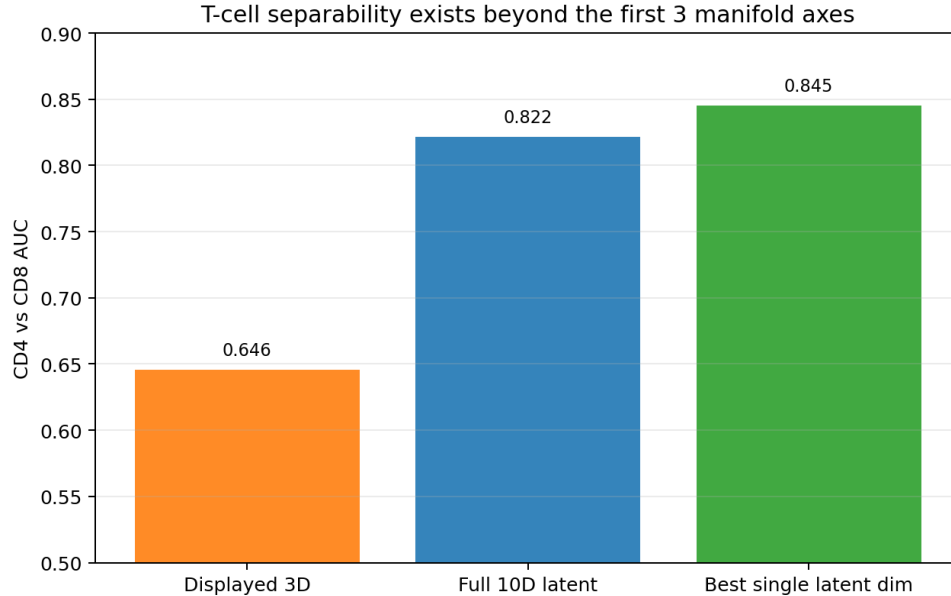


Figure 12: T-cell signal exists in latent space but is partially hidden in default 3D projection. The T-cell lens exposes this information for visualization.

- **dim 2:** strongest B/plasma contrast (AUC 0.990) and moderate developmental-depth loading ($|\rho| = 0.381$ to HSC graph distance).
- **dim 3:** strongest erythroid trajectory signal among dims 1–3 (erythroid-path $|\rho| = 0.631$), with moderate B/plasma loading (AUC 0.854).

CD4/CD8 separation is concentrated outside the default first three axes, peaking at **dim 4** (AUC 0.845); monocyte-vs-macrophage separation peaks at **dim 8** (AUC 0.907). The strongest global stage/branch structure appears at **dim 9** (stage η^2 0.952, branch η^2 0.883).

S25. Flatness and ripple structure

The manifold is predominantly flat in 3D but contains structured residual curvature. When projected to 3D, the manifold is nearly planar: the best-fit 2D plane explains 99.25% of the 3D variance in the external map (97.17% internally). However, the residuals are not random noise. After removing the dominant plane and any smooth quadratic trend, the remaining deviations show statistically significant periodic (ripple-like) structure (external $R^2 = 0.171$, $p = 0.0033$; internal $R^2 = 0.194$, $p = 0.0033$).

This structure persists in the full 10D latent space. We tested each residual axis (after removing the two dominant principal components) for similar periodic structure. In the internal 10D space, all 8 tested residual axes showed significant periodicity; in the external space, 5 of 8 were significant after multiple-testing correction. The first two principal components captured most but not all variance (internal 89.3%, external 78.4%), consistent with a compact but genuinely higher-dimensional manifold rather than a simple 2D surface.

Calibration null check. To verify that this test does not produce false positives on arbitrary high-dimensional point clouds, we generated a synthetic null dataset matched to the external 10D space in mean and covariance but with no biological structure. This null produced zero significant

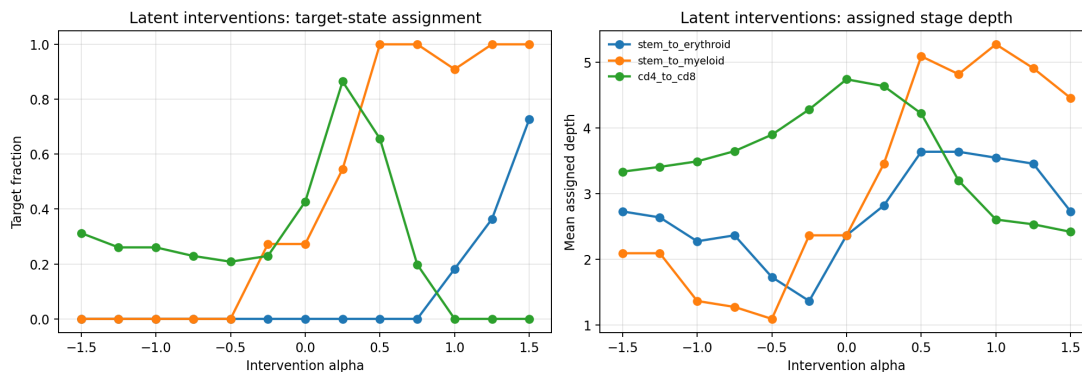


Figure 13: Phase-2 latent intervention sweeps. Positive monotonic shifts are strongest for stem→myeloid and stem→erythroid directions.

residual axes, confirming that the detected periodicity reflects real geometric structure in the manifold.

S26. Phase-2 deepening results

Latent interventions recover expected developmental directions. On strict non-overlap external anchors, stem→myeloid intervention showed strong monotonic enrichment ($\rho = 0.928$, $p = 4.9 \times 10^{-6}$, target fraction 0.00 → 1.00). Stem→erythroid also showed a strong shift ($\rho = 0.739$, $p = 0.0039$, target fraction 0.00 → 0.727). CD4→CD8 intervention was weaker and non-significant ($\rho = -0.518$, $p = 0.070$), consistent with subtype-local complexity.

Branch topology is preserved internally and partially externally. In the internal manifold, the hematopoietic stem cell (HSC) region serves as the root node with connections to four major lineages, six branching points, and complete reachability to all terminal cell types. In the external non-overlap panel, the HSC root structure is preserved (three connections, five branching points) but reachability to terminal types is incomplete (57.1%), likely reflecting the sparser external anchor coverage.

Biological interpretation of the residual curvature remains open. Despite the statistically significant periodic structure detected above, we could not assign biological meaning to specific residual axes. Associations between the periodic residual axes and a curated erythroid gene-program set did not survive multiple-testing correction (0/5 significant at BH-FDR $q \leq 0.05$). Whether this residual geometry encodes additional lineage-specific information remains an open question for future work.

S27. Sparse factorization

Starting from the selected **top1 + rank64** model, we applied a hard pruning grid over retained factor count and per-factor gene support size. The strongest sparse point (16 factors, 60 genes per factor, 10D with MLP2 readout) keeps 16 of the rank64 parent factors and retains the top 60 read genes plus top 60 write genes per factor. This reduces the deployable artifact to 124,512 bytes with only 1,920 active operator weights ($\sim 47\times$ smaller than dense compact top1). However, it no longer defines a new accuracy frontier: in the repeated 12-split audit it was materially worse than the rank64 parent on at least 6/8 BH-corrected endpoints.

The sparse-specific necessity audit shows that the top four retained parent factors **f01**, **f02**, **f00**, and **f03** explain 68.9% of the total sparse ablation impact, while the top eight explain 87.2%. The

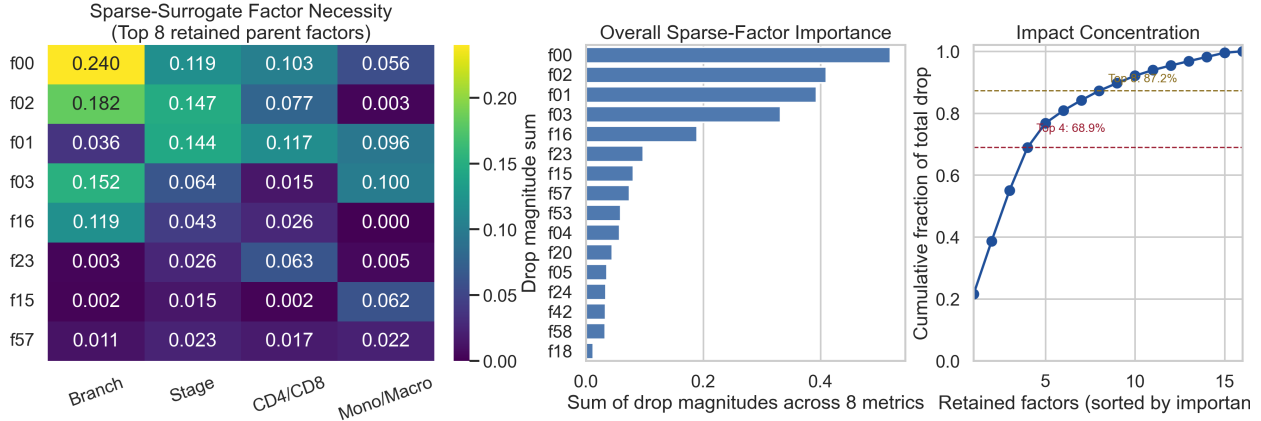


Figure 14: Fixed-probe leave-one-factor-out audit for the best sparse surrogate. The sparse model preserves the same mechanistic core as the rank64 parent: the top four retained factors explain 68.9% of total sparse ablation impact.

Table 20: Gene-program summary for the four core sparse-surrogate factors. Drop is the total pooled ablation impact. Read/write genes and enrichment are from cached local marker analysis. The same biological programs persist after hard-sparse pruning.

Factor	Role	Drop	Top read/write genes	Enriched programs
f01	Branch routing	0.430	R: EPB41, GBR1, VPEL3, GPX1, TAL001; W: DIF2R, EPB41, VPEL5, RBXP3L, RMT39	Classical and non-classical monocyte identity
f02	Lymphoid contrast	0.254	R: IL7R, GSTPL, DIF2R, ChrFTB, GPFC, FNL; W: HLA-DRA, MARCB9, AC96579.19, IGKC, IGLC1	Naïve CD8 ⁺ T-cell; thymic CD4 ⁺ ; B-cell lineage
f00	Stage ordering	0.280	R: IL7R, TENTSC, GSPT1, GVPC, GBK1, PRBX2; W: CSF3R, SLC2BA1, S100A8, ELR2, ACSL1, PRBB	Naïve CD8 ⁺ T-cell; T-regulatory; granulopoiesis
f03	Mono/macro struct.	0.241	R: LGALS3, BLC2L1, LV2, THBS1, C10A, BLVR8; W: VPEL1, ALPL, SLC28A3, FIG30R, ALTS, TENTSC	Macrophage; phagocyte; granulocyte/neutrophil

same qualitative biology persists: **f01** is still the dominant branch factor, **f00** remains a strong stage factor, and **f03** remains the main mono/macrophage factor.

Local marker-set enrichment of the retained sparse read/write supports makes those factors biologically explicit: **f00** contrasts granulocytic/neutrophil programs against T/NK markers; **f01** aligns with monocyte/macrophage programs; **f02** contrasts lymphoid/B-cell-like structure against T/NK; and **f03** separates monocyte/macrophage-like programs from granulocytic structure.

A subsequent learned/data-aware sparse fit at the same scale ($f = 16$, $k \in \{60, 80\}$) did *not* rescue the sparse boundary. The better learned point remained clearly worse than the rank64 parent and also worse than the naive hard sparse point on branch balanced accuracy and CD4/CD8 AUROC. The interpretability value remains concentrated in the rank64 core and in the explicit hard-sparse boundary model.

S28. Rank64 versus sparse core comparison

A direct comparison of the four core factors across the rank-64 and hard-sparse factorizations confirms that the same biological programs survive aggressive compression. Factors **f01**, **f02**, and **f03** retain identical top-ranked genes (both read and write sets) after sparsification, while **f00** preserves one gene set but changes the other, reflecting the information loss from pruning. Despite the smaller sparse model no longer matching the rank-64 parent on classification accuracy, both factorizations encode the same task-specialized pattern: **f01** dominates branch classification, **f02** separates lymphoid subtypes (B-cell versus T/NK), **f00** carries the strongest developmental-stage

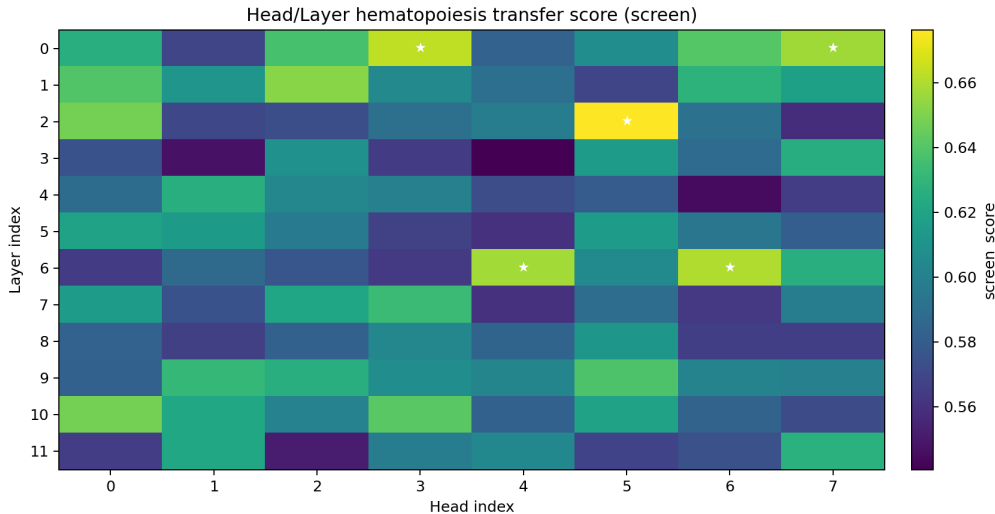


Figure 15: Head/layer attribution screen across all 96 scGPT attention units. Color shows external transfer screen score; stars mark top-ranked units.

Table 21: Top single heads after full refit on internal anchors and zero-shot evaluation on strict non-overlap external anchors.

Unit	Corr _{resid}	Trustworthiness	CD4/CD8 AUC _{3D}	Mono/Macro AUC _{3D}
L2H5 (screen rank 1)	0.634	0.985	0.711	0.873
L0H3 (screen rank 2)	0.627	0.981	0.743	0.769
L6H6 (screen rank 3)	0.621	0.984	0.765	0.867
L6H4 (screen rank 4)	0.610	0.986	0.765	0.810
L0H7 (screen rank 5)	0.636	0.977	0.746	0.765

signal, and **f03** isolates monocyte/macrophage structure.

S29. Head/layer attribution details

The 96-unit attribution scan showed that transferable hematopoiesis geometry is distributed across multiple layers, with clear high-performing units. The screen-selected best unit was **Layer 2 / Head 5** (L2H5). After full refit, L2H5 reached external corr 0.636, residualized corr 0.634, and trustworthiness 0.985, with 3D subtype AUCs 0.711 (CD4/CD8) and 0.873 (monocyte/macrophage).

Relative to pooled transferable heads, the best single head is competitive for global stage-distance alignment (L2H5 residualized corr 0.634 vs pooled-anchor 0.605, pooled-cell 0.612, and conservative-hybrid 0.632). However, subtype separation remains better in pooled/hybrid variants (CD4/CD8 AUC 0.911 in conservative hybrid vs 0.711 in L2H5), supporting a two-view interpretation: single heads can carry strong global geometry, while pooled objectives can better expose fine subtype margins.

S30. Factor ablation details (core-sufficiency and interactions)

Necessity does not imply sufficiency. We ran a fixed-probe core-sufficiency test on cumulative subsets **{f01}**, **{f01, f02}**, **{f01, f02, f00}**, and **{f01, f02, f00, f03}** over the same 12 grouped donor-holdout

Table 22: Best subset from the exhaustive 15-subset interaction sweep for each audited endpoint. Every listed subset remains BH-significantly below the intact rank64 model.

Endpoint	Best subset	Size	Best / intact
Branch BA	{ f01 , f02 , f00 , f03 }	4	69.7%
Branch F1	{ f01 , f02 , f00 , f03 }	4	71.7%
Stage BA	{ f01 , f02 , f00 , f03 }	4	44.0%
Stage F1	{ f01 , f02 , f00 , f03 }	4	45.5%
CD4/CD8 AUROC	{ f02 , f00 , f03 }	3	83.1%
CD4/CD8 BA	{ f01 , f00 , f03 }	3	82.9%
Mono/Macro AUROC	{ f01 , f03 }	2	94.9%
Mono/Macro BA	{ f01 , f03 }	2	92.3%

splits. The four-factor core is the strongest of these subsets, but it still falls well short of the intact rank64 model: pooled means are branch balanced accuracy 0.572 versus 0.820, stage balanced accuracy 0.191 versus 0.435, CD4/CD8 AUROC 0.699 versus 0.846, and mono/macro AUROC 0.834 versus 0.951, with BH-significant losses on all 8 endpoints.

The sweep is clearly non-additive: adding **f00** before **f03** sharply damages mono/macro performance (mono/macro AUROC 0.381 for {**f01**, **f02**, **f00**}), and only partial recovery appears once **f03** is restored.

The exhaustive 15-subset interaction sweep resolves this further. No pair or triple closes the gap to the intact rank64 model: all 15 subsets remain BH-significantly worse on all 8 endpoints. But different subsets dominate different tasks. Branch and stage are best recovered by the full four-factor set; mono/macro is best recovered by the pair {**f01**, **f03**} (mono/macro AUROC 0.902, balanced accuracy 0.803); and the strongest CD4/CD8 recovery comes from triples centered on **f00** and **f03** (CD4/CD8 AUROC 0.703).

S31. Dimension-wise functional audit

Cell-trained head dimension audit. When training the adaptor head on individual cells rather than anchors, the overall stage and branch information remains strong (best stage η^2 : dim 3, 0.924; best branch η^2 : dim 8, 0.835), but the distribution of subtype information across dimensions changes substantially. CD4/CD8 separation now peaks at **dim 10** (AUROC 0.902) rather than dim 4 (0.845 in the anchor-trained head). The first three dimensions—which determine the default 3D visualization—carry much more T-cell subtype contrast in the cell-trained head (max CD4/CD8 AUROC among dims 1–3: 0.847 vs 0.607; max mono/macro AUROC: 0.936 vs 0.659), at the cost of reduced B/plasma dominance in those early dimensions (0.910 vs 0.990).

Temporal differentiation is distributed, not single-axis. In the anchor-trained head, the strongest global depth proxy loads on dim 7 ($\rho = 0.452$ to HSC graph distance), while lineage-specific ordering peaks on different axes (erythroid on dim 10, $|\rho| = 0.672$; monocyte/macrophage on dim 8, $|\rho| = 0.731$; B→plasma on dim 2, $|\rho| = 0.875$). In the cell-trained head, depth loading shifts to dim 9 ($\rho = 0.640$), again with lineage-specific maxima on different dimensions.

Composite temporal axis search. A ridge-regularized linear axis over LET-10D using six standardized temporal components reached Spearman $\rho = 0.623$ to the composite target and $\rho = 0.627$ to HSC depth ($p = 5.0 \times 10^{-4}$, one-sided permutation), with dominant loadings on dims 9, 2, 5, and 4.

Important caveat: dimensions are not independent factors. The latent axes are correlated in both variants (mean absolute off-diagonal correlation: anchor-trained 0.493, cell-trained 0.400).

Interpretation should treat dimensions as a mixed/distributed code rather than one-factor-per-axis.

S32. H38 goal and biological target

To test whether the discovery protocol generalizes beyond hematopoiesis, we ran an independent branch (H38) targeting *intercellular communication geometry* in scGPT. The target ruler differed from H65: instead of developmental-stage distances, H38 used curated interaction-path structure derived from OmniPath [61] and ligand-receptor attention-flow summaries. The question was whether a compact manifold fit to this signal could pass strict baseline and transfer checks under the same no-cheating policy used in the main study.

S33. H38 canonical setup

H38 used an internal anchor panel of 104 anchors constructed from 30 selected ligand-receptor interaction-path pairs (square-root-weighted distances). We evaluated three random seeds, two manifold-learning methods (geodesic MDS and Isomap), and three neighborhood sizes ($k \in \{10, 15, 20\}$). The best internal setting was seed 43 with geodesic MDS at $k = 10$.

Median internal summary across settings:

- trustworthiness = 0.9082 (min/max 0.8910/0.9282),
- geodesic-anchor correlation = 0.8277 (min/max 0.8256/0.8297),
- blocked-permutation $p = 0.0005$,
- manifold-minus-PCA2 baseline margin = +0.0544.

The canonical internal run passed both primary and strict baseline gates, with stable fragility controls (subsample sign consistency = 1.0, cell-type-holdout sign consistency = 1.0).

S34. H38 first external check: strong association but strict-baseline failure

The first zero-shot external replication used a preprocessed immune panel (20,000 cells, 102 tissue-level anchors after requiring at least 40 cells per anchor group). It remained strongly significant by correlation and permutation test, but failed strict baseline gates:

- trustworthiness median = 0.9373,
- correlation median = 0.9086,
- blocked-permutation $p = 0.0005$,
- median margin vs PCA2 = -0.0736 (non-passing under strict baseline policy).

This reproduced the same pattern observed earlier in our broader loop: high raw association alone is insufficient for a positive claim unless baseline margins also pass.

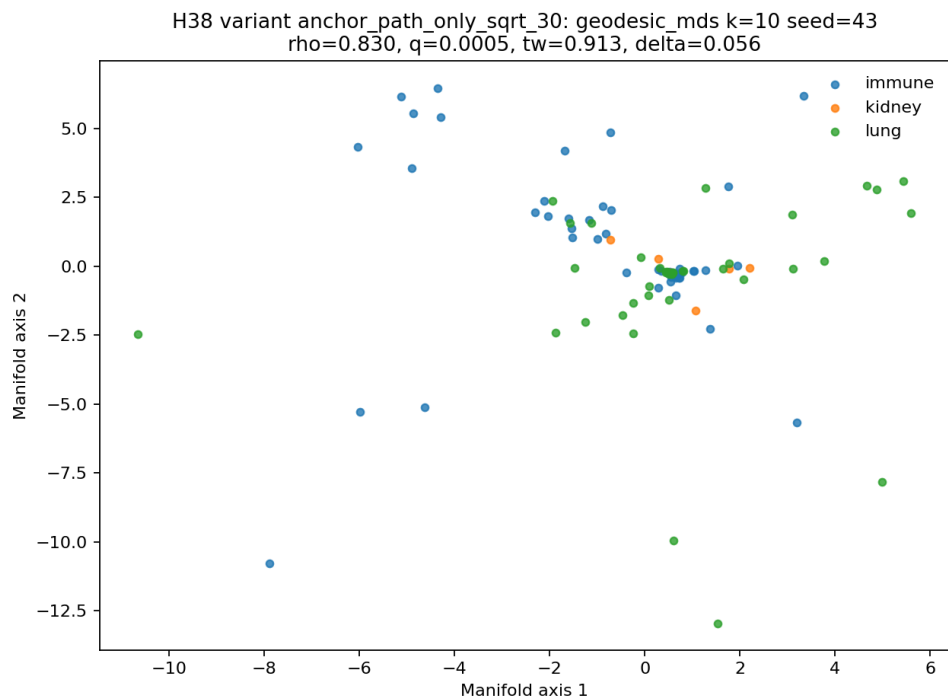


Figure 16: **H38 internal canonical manifold.** Best internal embedding using 30 interaction-path pairs with square-root-weighted distances. This branch captures a structured intercellular-communication axis system distinct from the hematopoietic developmental geometry in the main text.

S35. H38 negative controls and axis-level interpretation

Negative controls showed that not all null manipulations were cleanly separated from the observed score under this first external setup, especially for strict baseline margins:

- flow-gene permutation: empirical $p_{corr} = 0.0732$, $p_{\Delta} = 0.2439$,
- random hop-matched pairs: empirical $p_{corr} = 0.3659$, $p_{\Delta} = 0.9756$.

Axis interpretation remained biologically meaningful, with strongest module associations in cytokine/chemokine, IL1-axis, coagulation/ECM, and lipid/metabolic programs (module-pair counts 8, 4, 17, 2, respectively). For example, axis 1 showed strong broad-class structure ($\eta^2 = 0.735$) and opposite-direction associations with cytokine/chemokine ($\rho = -0.549$) and lipid/metabolic ($\rho = 0.566$).

S36. H38 iterative rescue without target-dataset leakage

We ran an iterative rescue track (v4→v11), keeping external evaluation frozen and avoiding any target-dataset optimization. Table 23 summarizes the progression.

The final v11 run expanded internal training coverage from narrow subsets to raw Tabula immune+lung+kidney anchors:

- internal anchors: 392,

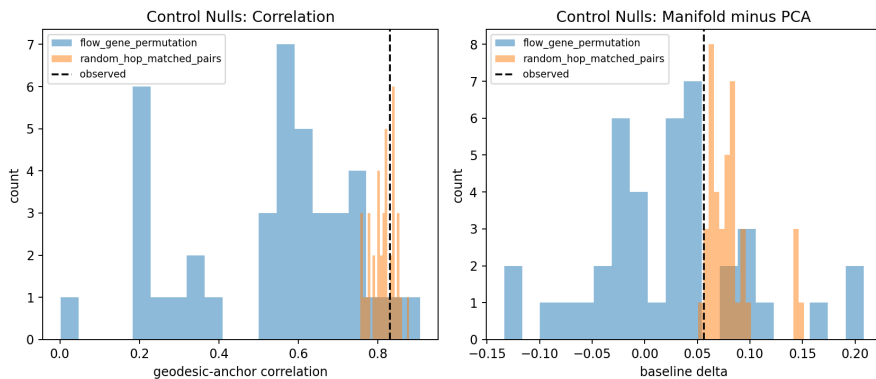


Figure 17: **H38 negative-control distributions.** Observed H38 alignment was not cleanly separated from all control draws under early external conditions, motivating the rescue program below.

Table 23: H38 rescue progression on external zero-shot evaluation (minimum 40 cells per anchor group).

Run (key change)	External corr	Δ vs PCA2
v4 (pair hygiene + hard negatives)	0.8850	-0.0909
v5 (cell-trained transfer head)	0.9624	-0.0199
v7 (metric head + cleaned pair set + ensemble)	0.9707	-0.0061
v9 (cell-metric head + ensemble)	0.9800	+0.0032
v10 (MLP-geom/dim6 extras)	0.9747	-0.0021
v11 (raw diverse 100k-cell internal training + ensemble)	0.9825	+0.0057

- sampled training cells: 100,000 (target met exactly),
- diversity: 23 donors, 58 cell types, 3 tissues.

On the external panel (minimum 40 cells per anchor), v11 produced:

- anchor baseline: corr 0.8862, Δ vs PCA2 = -0.0906 ,
- cell-metric head: corr 0.9776, Δ vs PCA2 = $+0.0008$,
- ensemble head: corr 0.9825, Δ vs PCA2 = $+0.0057$,
- blocked-permutation $p = 0.0005$.

This closes the main external-validation gap for H38 under the same strict criteria used in the main paper: no target-dataset information was used during any rescue iteration.

S37. H38 practical interpretation and limits

H38 supports a complementary biological signal family to hematopoiesis. While H65 organizes developmental branch structure, H38 emphasizes communication-program geometry (cytokine/chemokine- and IL1-linked axes with ECM/coagulation and lipid/metabolic contrasts). The rescue sequence also clarifies a methodological point: transfer quality depended strongly on internal training coverage and diversity, not on loosening gates.

At the same time, H38 remains secondary evidence relative to H65:

- it required a longer rescue path to pass strict external margins,
- the biological interpretation of its axes is suggestive but has not been validated with the same intervention experiments used for H65,
- classification benchmark results are mixed (for example, the 2D manifold embedding outperformed a 2D PCA baseline but not a 6D PCA baseline on grouped macro-F1: 0.482 vs 0.464 vs 0.531).

We therefore treat H38 as a successful generalization case: the discovery and extraction protocol transferred to a biologically distinct manifold family (intercellular communication rather than developmental hierarchy) and achieved strict external validation after expanding internal training coverage, but with lower overall maturity than the primary hematopoiesis result.